

From Kondo Lattices to Kondo Superlattices

Masaaki Shimozawa¹, Swee K. Goh², Takasada Shibauchi³, and Yuji Matsuda⁴

¹*The Institute for Solid State Physics (ISSP), The University of Tokyo, Kashiwa, Chiba 277-8581, Japan*

²*Department of Physics, The Chinese University of Hong Kong, Shatin, New Territories, Hong Kong, China*

³*Department of Advanced Materials Science, University of Tokyo, Kashiwa, Chiba 277-8561, Japan*

⁴*Department of Physics, Kyoto University, Kyoto 606-8502, Japan*

(Dated: February 15, 2019)

Realizing new classes of ground states in strongly correlated electron systems continues to be at the forefront of condensed matter physics. Heavy-fermion materials, whose electronic structure is essentially three-dimensional, are one of the most suitable systems for obtaining novel electronic states because they demonstrate many fascinating properties associated with many-body effects. Recently, a state-of-the-art molecular beam epitaxy technique has been developed to reduce the dimensionality of the heavy electrons by fabricating the artificial superlattices including the heavy fermion compounds, which can produce new type of electronic states present in two-dimensional heavy fermion system. In artificial superlattices of the antiferromagnetic heavy fermion compound CeIn₃ and the conventional metal LaIn₃, the magnetic order is suppressed by reducing the thickness of the CeIn₃ layers. The two-dimensional confinement of heavy fermion also leads to the enhancement of the effective electron mass and the deviation from the standard Fermi liquid electronic properties, which both are associated with the dimensional tuning of quantum criticality. In superconducting superlattices of heavy fermion superconductor CeCoIn₅ and nonmagnetic metal YbCoIn₅, signatures of superconductivity are found even at the thickness of one unit cell layer of CeCoIn₅. The most remarkable feature of this extremely two-dimensional heavy fermion superconductor is that the thickness reduction of the CeCoIn₅ layers drastically changes the temperature and angular dependencies of the upper critical field. This result would be attributed to a significant suppression of the Pauli pair-breaking effect through the local inversion symmetry breaking at the interfaces of CeCoIn₅ block layers. The importance of the inversion symmetry breaking in this system has also been supported by site-selective nuclear magnetic resonance spectroscopy, which can resolve spectroscopic information from each layer, separately, even within the same CeCoIn₅ block layer. In addition, recent experiment of CeCoIn₅/YbCoIn₅ superlattices have shown that the degree of the inversion symmetry breaking and, consequently Rashba splitting are controllable, which offers the prospect of achieving even more fascinating superconducting states. These Kondo superlattices, thus, pave the way for exploring unusual metallic and superconducting states.

CONTENTS

I. Introduction	2	A. Characterization of CeIn ₃ /LaIn ₃ superlattices	9
II. Heavy fermion compounds Ce _n T _m In _{3n+2m}	3	B. Suppression of Néel temperature with the dimensionality reduction	10
A. Antiferromagnetic heavy fermion CeIn ₃	3	C. 2D antiferromagnetic QCP	10
B. Heavy fermion superconductor CeCoIn ₅	3	V. 2D heavy fermion superconductor of CeCoIn ₅ /YbCoIn ₅ superlattices	11
1. 3D electronic, magnetic and superconducting properties	3	A. Characterization of CeCoIn ₅ /YbCoIn ₅ superconducting superlattices	12
2. Non-Fermi liquid behavior	4	B. 2D heavy fermion superconductivity	12
3. Quantum critical point (QCP)	4	C. Enhancement of H_{c2}/T_c	13
4. Superconductivity	6	D. Local inversion symmetry breaking	15
5. Superconducting gap structure	6	1. Superconducting properties	15
6. Pauli-limited superconductivity, FFLO state and Q-phase	6	2. Magnetic properties	16
III. Experimental methods	7	VI. Controllable Rashba spin-orbit interaction in CeCoIn ₅ /YbCoIn ₅ superlattices	17
A. Molecular beam epitaxy (MBE) systems	7	A. Characterization of the modulated superlattices	17
1. Features of MBE technology	8	B. 2D superconducting state	18
2. MgF ₂ substrate	8	C. Block layer inversion symmetry breaking	18
B. 2D Kondo lattice	8	VII. Conclusion	19
C. Superconducting Kondo superlattices	8	Acknowledgments	20
IV. Tuning the quantum criticality in CeIn ₃ /LaIn ₃ superlattices	9		

I. INTRODUCTION

Strongly interacting quantum many-body systems are one of the central issues in modern physics. In condensed matter systems, such complex interactions between particles are responsible for intricate interplay between charge, spin and orbital degrees of freedom, giving rise to a variety of intriguing ground states, such as unconventional superconductivity, magnetically ordered states, and states exhibiting interesting charge and orbital orderings. These phases often coexist and compete with one another, resulting in complicated phase diagrams. Transition between these phases can be generally driven by external parameters including pressure, chemical doping or magnetic fields. Of particular interest is the case of driving a second order phase transition at zero temperature.¹⁻³ In the vicinity of such a zero-temperature transition point, called the quantum critical point (QCP), quantum fluctuations bring about a significant modification of the quasiparticle masses and scattering cross sections of the Fermi liquid. This leads to striking deviations from conventional Landau Fermi liquid description of metallic systems. Furthermore, superconductivity is often observed in the phase space near the QCP. Thus, strongly correlated electron systems, which host many fascinating physical phenomena and offer suitable platforms for exploring exotic physics resulting from quantum criticality, have attracted significant attention of condensed matter researchers.

Among the existing strongly correlated materials, the ground state with the strongest electron correlation effects is achieved in heavy-fermion compounds containing $4f$ or $5f$ electrons.⁴ In these systems, the f electrons which can couple with conduction electrons form a dense periodic array. This array is called a Kondo lattice and it is usually three dimensional (3D). These f electrons, which are localized at high temperatures, hybridize with the conduction electrons at low temperatures, thereby forming a very narrow conduction band. The quasiparticle effective mass of the narrow band is significantly enhanced, which sometimes reaches a value as large as 1000 times the free electron mass. The term “heavy fermion” is derived from this fact. In such heavy fermion systems, the magnetic moment of localized f electrons is quenched through the Kondo effect, leading to a nonmagnetic state. On the other hand, the localized f electron moments interact with each other via the Ruderman–Kittel–Kasuya–Yoshida (RKKY) interaction, which promotes magnetic ordering. The competition between the Kondo effect and the RKKY interaction is a key element in determining whether the ground state is a non-magnetic metal or a magnetically ordered state. Moreover, the interplay between spin, valence, and orbital degrees of freedom of the f electrons affects the electronic and magnetic states, leading to a rich variety of phenomena such as the coexis-

tence of superconductivity and ferromagnetism,^{5,6} multiple superconducting phases with different order parameter symmetries,⁷ reentrant superconductivity,⁸ multipolar ordering,^{9,10} and mix valence state.¹¹ Thus, the 3D Kondo lattice plays an important role in heavy fermion physics.

Generally, in low spatial dimensions, many-body correlation effects coming from the Coulomb interaction between electrons become more important and complex. Moreover, both thermal and quantum fluctuations are largely enhanced with a reduced dimensionality, thereby expanding the critical regions near the QCP. Thus, many-body effects that does not exist in three dimensions are expected to prevail in low dimensional systems. Indeed, two-dimensional (2D) systems exhibits anomalous properties such as high- T_c superconductivity in cuprates^{12,13} and iron-pnictides,^{14,15} metallic conduction in transparent oxides,¹⁶ high-capacitance in heterostructure forms, large thermopower,¹⁷ and quantum Hall effect.¹⁸ If Kondo lattices can be made 2D, even more fascinating ground states are expected to appear.

There have been attempts to realize heavy fermion systems with low dimensionalities. In particular, it is desirable to have a means to tune the dimensionality of heavy fermion systems to track the evolution of the strength of many-body interaction. One approach is to insert ‘block layers’ into a 3D Kondo lattice. This has been utilized in the growth of the bulk crystals of $CeTIn_5$ ($T = Rh, Co, \text{ or } Ir$),¹⁹⁻²¹ whose crystal structure comprises alternating layers of $CeIn_3$ and TIn_2 . According to the band structure calculation, the ‘block layers’ TIn_2 are less conductive than $CeIn_3$ layers.²² Therefore, $CeTIn_5$ can be treated as a quasi-two dimensional system. However, the largely corrugated Fermi surface sheets,²³ 3D-like antiferromagnetic fluctuations in the normal state,²⁴ and small anisotropy of upper critical fields,²⁵ all indicate that the electronic, magnetic, and superconducting properties of $CeTIn_5$ are essentially 3D rather than 2D. Another example of 2D Kondo systems is the bilayer 2D films of 3He fluid,²⁶ where the mass enhancement is observed near a QCP. Here the control parameter is the 3He density of the second layer, and thus it may involve different physics from f -electron based heavy fermions. Therefore, systematic dimensionality tuning heavy fermion systems is still lacking.

Recently, advances in thin films growth technology has led to the fabrication of artificial 2D structures with controlled atomic-layer thicknesses, providing a unique opportunity to explore novel phenomena in low dimensional systems with unprecedented control. For example, 2D electron gas,²⁷ magnetism,²⁸ and 2D superconductivity²⁹ are observed at the interface between insulating nonmagnetic oxides $LaAlO_3$ and $SrTiO_3$, which are believed to be closely associated with the interface electronic structure and film thickness. In another example, several peculiar features are observed in Hubbard superlattices of the antiferromagnetic Mott-Hubbard insulator $LaVO_3$ and the paramagnetic metal $SrVO_3$: a metal-insulator

transition,³⁰ room-temperature ferromagnetism with an insulating interface,³¹ a resistivity downturn resembling a Kondo coherent state,³² and so on. Thus, a wide variety of nanometric thin films and superlattices displays notable features due to low dimensionality and interfacial effect.

Very recently, a state-of-the-art molecular beam epitaxy (MBE) technique has been developed to reduce the dimensionality of the heavy electrons by fabricating multilayers of Ce-based heavy fermion materials sandwiched between conventional metals. In this report, we first examine the heavy fermion properties of the bulk CeIn₃ and CeCoIn₅, to set the scene for later discussions of “Kondo superlattices”. After that, we will discuss the artificial superlattices CeIn₃/LaIn₃,³³ which undergo a quantum phase transition tuned by the dimensionality of the Kondo lattice; and superconducting Kondo superlattices CeCoIn₅/YbCoIn₅³⁴ in which the superconducting and magnetic properties can be substantially modified by tweaking the degree of spatial inversion symmetry breaking,^{35–37} achieved through a careful design and fabrication of superlattices with desirable layer thicknesses.

II. HEAVY FERMION COMPOUNDS

$Ce_nT_mIn_{3n+2m}$

The intensively studied heavy fermion compounds CeIn₃ and CeCoIn₅ belong to the series of compounds with general stoichiometry $Ce_nT_mIn_{3n+2m}$ (T is a transition metal element, $n = 1, 2$, or ∞ , and $m = 0, 1$ or 2).³⁸ These compounds, which are built of alternating n layers of CeIn₃ and m layers of TIn_2 stacked along the tetragonal c -axis, are characterized by the interplay of antiferromagnetic order, unconventional superconductivity, and quantum criticality. For example, CeIn₃,³⁹ CeRhIn₅,¹⁹ and CePt₂In₇⁴⁰ show the antiferromagnetic (AFM) state at ambient pressure. By applying hydrostatic pressure, the AFM order is suppressed, and the superconductivity emerges near the QCP. In other examples, namely CeCoIn₅,²⁰ CeIrIn₅,²¹ and Ce₂PdIn₈,⁴¹ an unconventional superconducting state develops from an anomalous normal state which displays the breakdown of Landau Fermi liquid behavior. Thus, the $Ce_nT_mIn_{3n+2m}$ series appears to be an excellent playground for the investigation of magnetism, superconductivity, and quantum criticality in heavy fermion systems. In this report, CeIn₃ and CeCoIn₅ are used for studying the effect of dimensionality reduction on antiferromagnetism and unconventional superconductivity in heavy fermion systems.

A. Antiferromagnetic heavy fermion CeIn₃

CeIn₃ has a cubic AuCu₃-type crystal structure, the simplest crystal structure among the $Ce_nT_mIn_{3n+2m}$ family. At ambient pressure, this compound undergoes an antiferromagnetic (AFM) transition at a Néel

temperature $T_N = 10$ K with the ordered moment of $\sim 0.5\mu_B/Ce$ and the commensurate wave-vector $\mathbf{Q} = (1/2, 1/2, 1/2)$.^{42,43} The 3D AFM state is suppressed monotonically by applying pressure, and a superconducting phase appears with a maximum $T_c \sim 0.2$ K near a critical pressure of $P^* \approx 2.5$ GPa.^{39,44} Around a putative AFM QCP, the coexistence of AFM order and superconductivity is reported,⁴⁵ which implies that the superconductivity may be mediated by magnetic interactions rather than by phonons. Above the superconducting dome, the resistivity strongly deviates from the Fermi liquid behavior, $\rho(T) \sim T^\alpha$ with $\alpha = 2$, and α approaches 1.6 at the critical pressure where $T_N \rightarrow 0$. This exponent is close to the expected value of 3/2 in the presence of scattering by 3D antiferromagnetic fluctuations,⁴⁶ indicating the existence of 3D AFM QCP. Thus, CeIn₃ appears to be an ideal candidate for understanding the relation between magnetism, unconventional superconductivity, and quantum criticality. Furthermore, the relatively simple electronic and magnetic structures make CeIn₃ particularly appealing.

B. Heavy fermion superconductor CeCoIn₅

The heavy fermion compound CeCoIn₅ exhibits superconductivity at 2.3 K, which is the highest transition temperature among the Ce-based heavy fermion systems. CeCoIn₅ has attracted much interest because of the anomalous normal state transport and superconducting properties such as non-Fermi liquid (NFL) behavior, quantum critical point (QCP), $d_{x^2-y^2}$ superconducting gap symmetry, strong Pauli effect, a possible Fulde-Ferrell-Larkin-Ovchinnikov (FFLO) state, and unusual coexistence of superconductivity and magnetic order at low temperatures and high fields. In the following, the detailed physical properties of CeCoIn₅ are described.

1. 3D electronic, magnetic and superconducting properties

CeCoIn₅ has a tetragonal HoCoGa₅-type crystal structure comprising alternating layers of CeIn₃ and CoIn₂ stacked along the c -axis. Such structural arrangement might imply that CeCoIn₅ is a 2D variant of CeIn₃. However, all the electronic, magnetic, and superconducting nature of CeCoIn₅ are found to be rather 3D instead of purely 2D.

Firstly, the de Haas-van Alphen (dHvA) measurements suggest that the main Fermi surface sheet with the cyclotron mass $m_c^* = 87m_0$ is highly corrugated,²³ which is significantly different from the cylindrical Fermi surface expected for 2D systems. This result indicates that the electronic structure is, if anything, 3D rather than 2D. Secondly, inelastic neutron scattering measurements detected the presence of magnetic fluctuations at the commensurate wavevector $\mathbf{Q} = (1/2, 1/2, 1/2)$.⁵² Moreover, the nuclear spin relaxation rate exhibits a

TABLE I. Temperature dependences of the physical properties in both Fermi liquid and CeCoIn₅. The Landau Fermi liquid theory has been reported to break down in CeCoIn₅.

	ρ	C/T	$\chi (\mathbf{H} \parallel c)$	R_H	$1/T_1$	β/T
Fermi liquid	T^2	const.	const.	const.	T	const.
CeCoIn ₅	T (Ref. 47)	$-\ln T$ (Ref. 20)	$T^{-\alpha}$, ($\alpha < 1$) (Ref. 48)	$1/T$ (Ref. 49)	$T^{1/4}$ (Ref. 50)	$1/T$ (Ref. 51)

temperature dependence of the form $1/T_1 \sim T^z$ with $z = 1/4$,⁵³ which is intermediate between $z = 0$ and $1/2$ for 2D- and 3D-AFM instability, respectively. Therefore, both experimental results provide the evidence that a rather isotropic AFM fluctuations develop in CeCoIn₅. Thirdly, anisotropy of the upper critical field is small ($H_{c2}^{H\parallel ab}/H_{c2}^{H\perp ab} \sim 2.4$)²⁵ compared to the case of 2D superconducting systems, which means that anisotropic 3D superconductivity is realized in CeCoIn₅. Thus, considering all these factors, CeCoIn₅ should be treated as an ‘‘anisotropic’’ 3D heavy fermion compound at best.

2. Non-Fermi liquid behavior

In conventional metals, the low-energy physics of the system can be described by Fermi liquid theory. As per this theory, the physical properties such as electrical resistivity, specific heat, magnetic susceptibility, Hall coefficient, and nuclear spin relaxation rate exhibit characteristic temperature dependence; *i.e.*, (1) the electrical resistivity ρ varies as T^2 ; (2) the specific heat divided by temperature C/T is a constant; (3) the magnetic susceptibility χ tends to a constant Pauli-like value; (4) the Hall coefficient R_H is independent of temperature; (5) the nuclear spin relaxation rate $1/T_1$ is proportional to T ; and (6) the volume thermal expansion coefficient β/T is constant. However, the standard Fermi liquid theory has been reported to break down in CeCoIn₅.

This non-Fermi liquid (NFL) behavior is commonly manifested as the temperature dependences of the physical properties that deviate qualitatively from conventional Fermi liquid behavior. In fact, NFL behavior in CeCoIn₅ can be observed in many ways listed in the Table I. For example, the resistivity shows $\rho \sim T$,⁴⁷ the specific heat exhibits $C/T \sim -\ln T$,²⁰ the magnetic susceptibility χ diverges with decreasing temperature,⁴⁸ the amplitude of R_H increases drastically as $1/T$,⁴⁹ the nuclear spin relaxation rate follows $1/T_1 \sim T^{1/4}$,⁵⁰ and the volume thermal expansion coefficient β/T diverges as $1/T$.⁵¹ Thus, the temperature dependences of ρ , C/T , χ , R_H , $1/T_1$, and β/T are qualitatively different from those of a Fermi liquid (see table I). This result would be attributed to strong fluctuations associated with the AFM QCP, as described in the following topic.

3. Quantum critical point (QCP)

The NFL behaviors of CeCoIn₅ at zero field and ambient pressure imply the presence of a QCP nearby. Key information about the QCP is also provided by both (a) the pressure and (b) magnetic field dependences of the physical properties. Until now, many experiments performed at high-pressure and/or high-field suggest that CeCoIn₅ is very close to an AFM QCP. The following are the details of these experiments.

(a) Pressure dependence

According to the resistivity measurements, the NFL behavior is suppressed and a Fermi liquid state with $\rho = \rho_0 + AT^2$ is recovered with increasing pressure.⁴⁷ At a critical pressure of $P^* \approx 1.6$ GPa, a rapid change in the residual resistivity ρ_0 and the coefficient A is observed. Since both ρ_0 and A are expected to be enhanced on approaching the QCP due to the strong fluctuations, this change indicates that CeCoIn₅ is located very close to the QCP at ambient pressure. In fact, it is known that Cd doping induces an AFM order in CeCoIn₅,⁵⁶ in which Cd doping appears to mimic the effect of a negative pressure, although the changes in carrier density and disorder are also caused by Cd substitution. Moreover, it has been reported that the unit cell volume of CeCoIn₅ at ambient pressure is equivalent to that of the isostructural antiferromagnetic compound CeRhIn₅ at $P = 1.6$ GPa,⁵⁷ which is smaller than but close to $P_c \sim 1.75$ GPa where $T_N \rightarrow 0$. In the zero-field P - T phase diagram (Fig. 1(a)), the shape of the superconducting dome in CeCoIn₅ also coincides with that in the isostructural antiferromagnetic compound CeRhIn₅⁵⁸ when it is assumed that CeCoIn₅ at ambient pressure is equivalent to CeRhIn₅ at 1.6 GPa. These results reinforce the speculation that the AFM QCP may be in CeCoIn₅ at an inaccessible slightly negative pressure.

This assumption is also supported by the specific heat⁵⁹ and dHvA measurements,⁶⁰ which suggest that CeCoIn₅ is pushed away from the QCP under pressure because the effective mass decreases with increasing pressure. Furthermore, the Hall coefficient measurements point out that the enhancement of $|R_H|$ at low temperatures is drastically suppressed at high pressure,⁶¹ implying the suppression of the fluctuations associated with the AFM QCP. Such a change in the magnetic fluctuation is directly observed by the nuclear quadrupole res-

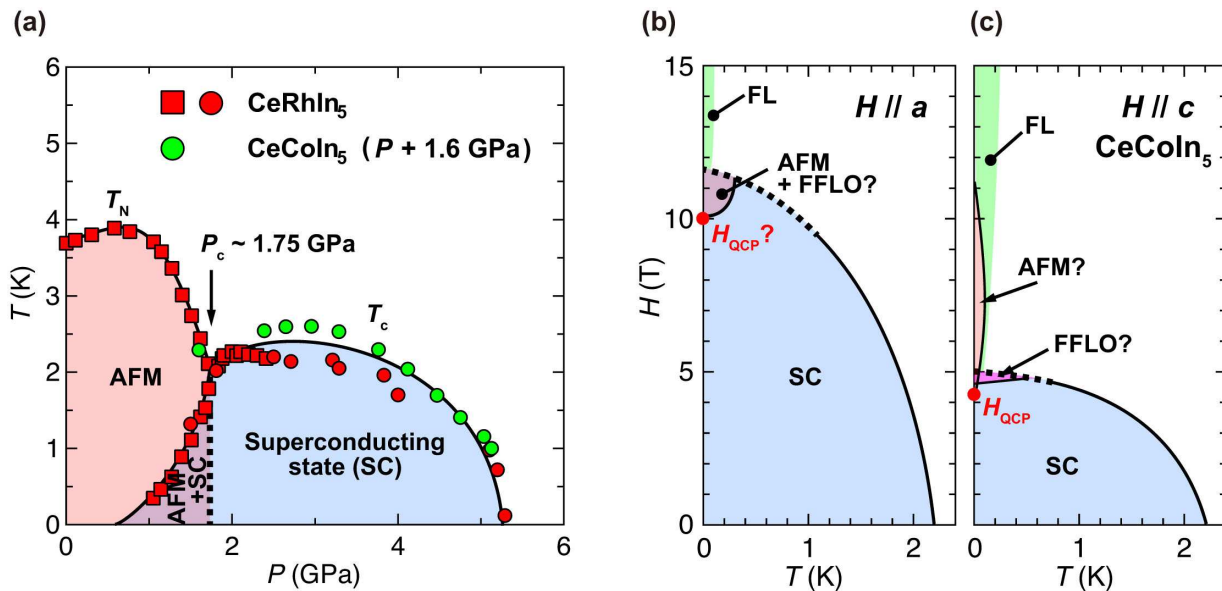


FIG. 1. Schematic representation of the phase diagrams. (a) Schematic P - T phase diagram at zero magnetic field for CeRhIn_5 and CeCoIn_5 . The pressure axis for CeCoIn_5 has been shifted by 1.6 GPa to reflect its smaller unit cell volume relative to that of CeRhIn_5 . The experimental data are taken from the specific heat measurements of CeRhIn_5 ⁵⁴ (red squares) and resistivity results of CeRhIn_5 ⁵⁵ (red circles) and CeCoIn_5 ⁴⁷ (green circles). T_N and T_c represent the Néel and superconducting transition temperatures, respectively. The dashed and solid lines represent the first-order and second-order phase boundaries, respectively. The AFM order coexists with superconductivity below P_c , while it is destroyed above P_c . (b),(c) Schematic H - T phase diagrams at ambient pressure of CeCoIn_5 for (b) $H \parallel a$ and (c) $H \parallel c$. H_{QCP} are slightly smaller than H_{c2} for both field directions. Field-induced AFM phase (Q-phase) was identified for $H \parallel a$, while there are no signature of an AFM state for $H \parallel c$.

onance (NQR). In CeCoIn_5 , the nuclear spin relaxation rate divided by the temperature, $1/T_1T$, is well described by $1/T_1T \propto (T + \theta_W)^{-3/4}$. As per spin fluctuation theory, the Weiss temperature θ_W is regarded as a scaling parameter which benchmarks the distance to the AFM QCP from the phase space location of the system. At ambient pressure, $\theta_W = 0.6$ K has been reported; however, θ_W increases with pressure,⁶² which again supports the existence of a pressure-induced AFM QCP close to ambient pressure in CeCoIn_5 .

(b) Magnetic field dependence

The low-temperature resistivity measurements of the normal state above the upper critical fields, $H_{c2} \sim 11.8$ T for $H \parallel ab$ ⁶³ and $H_{c2} \sim 4.95$ T for $H \parallel c$,⁶⁴ have revealed that a Fermi liquid state with $\rho = \rho_0 + AT^2$ is recovered at high magnetic field. The prefactor A exhibits a divergent behavior toward the critical field H_{QCP} for both $H \parallel ab$ and $H \parallel c$, which provides strong evidence for the presence of field-induced QCP. The quantum criticality was also detected in the measurements of specific heat,^{65,66} magnetization,⁴⁸ thermal transport,⁶⁷ Hall effect,⁶⁸ and thermoelectric coefficients.⁶⁹ What is remarkable is that H_{QCP} almost coincides with H_{c2} at ambient pressure, regardless of field orientation⁶³ or suppression of the superconducting state by Sn-doping.⁷⁰ This result naturally implies that the field-induced quantum criticality

might be inherently linked with the superconductivity. However, the H_{c2} transition has first-order character at low temperatures, as described later. Furthermore, the high-pressure resistivity measurements demonstrate that H_{QCP} is suppressed with increasing pressure faster than H_{c2} .⁷¹ These studies indicate that the superconducting fluctuations are unlikely to be responsible for the quantum critical behaviors at H_{QCP} .

The comparison between CeCoIn_5 and antiferromagnetic CeRhIn_5 would provide useful information on the nature of the critical fluctuations at H_{QCP} . In CeRhIn_5 at zero magnetic field, the AFM order is completely destroyed at the critical field of $P \sim 1.75$ GPa; however, the AFM phase is resurrected in the superconducting state under magnetic fields and expanded in magnetic fields higher than H_{c2} .^{25,72} This fact suggests that the field-induced quantum criticality in CeCoIn_5 is also likely associated with an as yet undetected AFM fluctuation because CeCoIn_5 is located close to the AFM QCP at zero field. Indeed, field-induced AFM phase (Q-phase) was recently found in CeCoIn_5 close to H_{QCP} for $H \parallel ab$,⁷³ as shown in Fig. 1(b). On the other hand, no signature of an AFM state was observed around H_{QCP} for $H \parallel c$. The AFM phase may possibly exist at ultra-low temperatures inaccessible to conventional dilution refrigerator (Fig. 1(c)).

4. Superconductivity

The zero-field-cooled magnetic susceptibility and resistivity provide clear evidence that CeCoIn₅ shows bulk superconductivity at $T_c = 2.3$ K.²⁰ The large $\gamma = C/T = 290$ mJ mol⁻¹K⁻² is observed just above T_c ,⁷⁴ indicating that the quasiparticle effective mass is significantly enhanced at low temperature. The steep initial slope of the upper critical field near T_c confirms that such heavy quasiparticles form Cooper pairs. Moreover, the jump size of the specific heat at T_c is remarkably large, and its value is $\Delta C/\gamma T_c \sim 4.5$, which suggests that CeCoIn₅ shows a very strong coupling superconductivity (the expected value for a weak coupling superconductor is only $\Delta C/\gamma T_c = 1.43$).

5. Superconducting gap structure

An unambiguous determination of the pairing symmetry in unconventional superconductors is essential to an understanding of their pairing mechanism and the origin of their superconductivity. In CeCoIn₅, the temperature dependence of the zero-field heat capacity ($C \propto T^2$) and the residual linear term in thermal conductivity ($\kappa \propto T$) indicate the presence of line nodes in the superconducting energy gap.⁷⁵ Moreover, the spin relaxation rate, $1/T_1$,⁵⁰ obtained by NQR measurements is approximately described by $1/T_1 \propto T^3$ law and no Hebel-Slichter coherence peak is observed at T_c , which is significantly different from that of conventional superconductors. These measurements thus provide strong evidence for unconventional superconductivity with line nodes in the superconducting gap. The penetration depth measurements also support this conclusion although the low- T exponent deviates from unity,^{76,77} which may be attributed to strong fluctuations arising from the QCP.⁷⁸

In unconventional superconductors, *i.e.*, those with non s -wave pairing states, the spin-part of the pairing wavefunction can have two types of pairing symmetry: spin-singlet pairing or spin-triplet pairing.¹¹⁵ In and ⁵⁹Co nuclear magnetic resonance (NMR) Knight shift^{50,79} and torque measurements⁸⁰ reveal the suppression of spin susceptibility below T_c , which implies that CeCoIn₅ is a singlet superconductor. This result is consistent with the observation of first-order superconducting to normal states transition, due to the Pauli pair-breaking effect, at high magnetic fields and low temperatures. Considering the existence of line nodes in the superconducting gap, it is established that the superconducting order parameter of CeCoIn₅ must possess a d -wave symmetry.

For CeCoIn₅, these line nodes can assume one of the two forms, namely $d_{x^2-y^2}$ or d_{xy} symmetry. The direction of the nodes has been measured using various techniques. In the thermal conductivity⁸¹ and specific heat measurements,⁸² a four-fold oscillation is clearly observed with a magnetic field rotating in the ab plane. The

location of these maximum values is consistent with a $d_{x^2-y^2}$ -wave symmetry order parameter. Point contact spectroscopy,⁸³ which observed the Andreev reflection signals in the normal metal/CeCoIn₅ junctions along two crystallographic orientations, [100] and [110], have also concluded that the gap symmetry is $d_{x^2-y^2}$. Moreover, small angle neutron scattering experiments have reported the presence of square vortex lattice,⁸⁴ whose orientation relative to the crystal lattice is consistent with the expectation for the $d_{x^2-y^2}$ -symmetry. Most recently, scanning tunneling microscopy measurements^{85,86} support these conclusions by measuring the response of superconductivity to various perturbations, through quasiparticle interference and local pair-breaking experiments. Taking into account these results from a wide range of measurements, the nodes in CeCoIn₅ are most consistently of the $d_{x^2-y^2}$ gap symmetry, which has implications that the AFM fluctuations are important for superconductivity. This observation is in qualitative agreement with NMR⁵³ and neutron scattering⁵² experiments which reported anisotropic spin fluctuations.

6. Pauli-limited superconductivity, FFLO state and Q -phase

Magnetic field destroys superconductivity through two mechanisms: the orbital pair-breaking and Pauli pair-breaking effects. In the former case, Cooper pairs are destroyed by the effect of Lorentz force, while in the latter case superconductivity is destroyed by the Zeeman splitting of spin singlet Cooper pairs. In the case of a superconductor with strong Pauli effect, it was predicted that the superconducting transition would change from second- to first-order below $T/T_c = 0.55$,^{87,88} but there had not been any conclusive experimental evidence supporting this conjecture for almost over 40 years. Recently, the first-order phase transition was, as far as we know, first observed in thermal conductivity measurements of CeCoIn₅,⁸¹ indicating that superconductivity is dominated by Pauli paramagnetism. This conclusion was also confirmed by the step-like features of the specific heat,^{65,89} magnetization,^{48,90} magnetocaloric,⁹¹ and thermal expansion measurements.^{92,93}

In CeCoIn₅ with strong Pauli effect, the Maki parameters, $\alpha_M \sim 4.6$ for $\mathbf{H} \parallel ab$ and $\alpha_M \sim 3.6$ for $\mathbf{H} \parallel c$, are substantially larger than the minimum required value of $\alpha_M = 1.8$ for realizing the spatially inhomogeneous Fulde-Ferrell-Larkin-Ovchinnikov (FFLO) state,^{94,95} where α_M represents the ratio of the orbital to Pauli limiting critical fields, $\alpha_M = \sqrt{2}H_{c2\perp}^{\text{orb}}(0)/H_{c2\perp}^P(0)$.⁹⁶ Additionally, CeCoIn₅ crystals can be made very pure,⁹⁷ thus the stringent requirement of ultrahigh purity for the stabilization of the FFLO state is comfortably satisfied. Therefore, the FFLO state is expected to be realized in CeCoIn₅. Up to date, signatures of a new superconducting phase have been observed by several experiments such as heat capacity,^{65,89}

ultrasound,⁹⁸ penetration depth,⁹⁹ and thermal conductivity measurements¹⁰⁰ at low temperatures in the vicinity of upper critical field H_{c2} for both $\mathbf{H} \parallel ab$ and $\mathbf{H} \parallel c$. This new phase exhibits properties that are consistent with the formation of the FFLO state, and hence CeCoIn₅ could indeed host the long sought-after FFLO phase after ~ 40 years of intensive search.

¹¹⁵In NMR measurements^{101,102} provide direct microscopic information on the low temperature, high magnetic field phase near H_{c2} in CeCoIn₅: (a) below H_{c2} , a new resonance peak appears with a small but finite intensity at higher frequency, and (b) its frequency coincides well with the resonance frequency obtained in the normal state. The first feature implies that the weak peak is unlikely to be generated by AFM ordering, because if AFM order develops, the alternating hyperfine fields would produce two inequivalent In(1) sites, which generates two resonance peaks with equal intensities. The second feature suggests that the higher resonance peak is a manifestation of a novel normal-state quasiparticle structure in the high-field-low-temperature region of the phase diagram. These observations point to the possibility of an FFLO state in CeCoIn₅.

The investigation of the presumed inhomogeneous superconducting state is further complicated by the recent observation of a field-induced long-range incommensurate AFM phase (Q-phase), detected by NMR/NQR^{103,104} and neutron scattering.^{73,105} This magnetically ordered state emerges only in the superconducting mixed state and is observed in the same high-field-low-temperature region of the phase diagram as the region where the FFLO state was proposed to exist. The ordering wave-vector $\mathbf{Q} = (0.45, 0.45, 1/2)$ is the same when \mathbf{H} is applied parallel to [100] and [110] crystallographic directions,¹⁰⁶ which is in contradiction with the predictions for the FFLO state. Several theoretical ideas have been proposed to account for this characteristic relationship between superconductivity and magnetism. Some ideas suggest that Q-phase is independent of a possible FFLO state¹⁰⁷ and, consequently, coexists with the nodal, $d_{x^2-y^2}$ -wave gap symmetry, whereas others emphasize that Q-phase is allowed to be stabilized because of the presence of the FFLO state.¹⁰⁸ Thus, it is still unclear whether this Q-phase replaces or coexists with a non-standard FFLO state, but recent NMR experiments at least reveal a quasiparticle density of states consistent with coexisting FFLO nodal planes and long range antiferromagnetic order.¹⁰⁹

III. EXPERIMENTAL METHODS

Our group has pioneered an MBE technique (Fig. 2) to fabricate artificial heavy fermion superlattices in a controllable fashion using layer-by-layer epitaxial growth of Ce-based materials. Such Kondo superlattices can essentially be regarded as a 2D Kondo lattice under some conditions. Recently, it has also become possible to tune

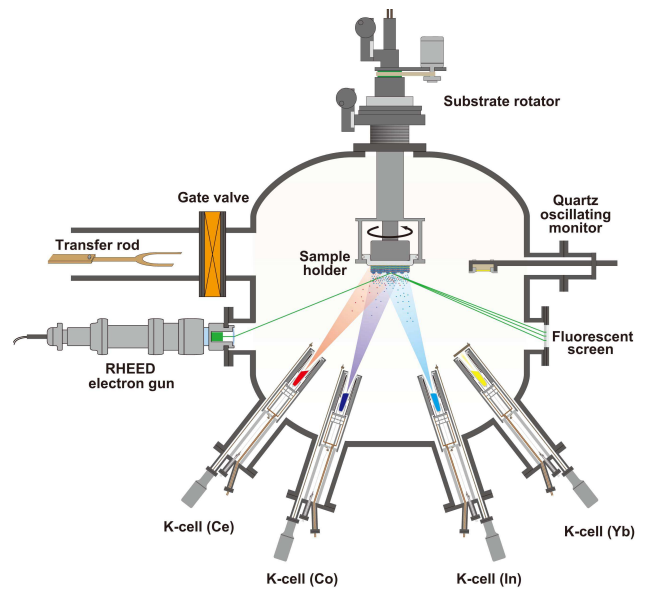


FIG. 2. Schematic view of an MBE system for fabrication of Kondo superlattices. The molecular beams are generated by heating solid materials placed in Knudsen cells (K-cells), which are then directed to the crystalline substrate surface. Due to the very large free mean path under ultra-high vacuum conditions, very few collisions occur between the particles. The substrate is placed on a sample holder, which is heated to the necessary temperature by resistive heaters. The deposition rate of each element is precisely controlled by a quartz oscillator thickness monitor. The MBE system is equipped with the RHEED, which is used for monitoring the morphology and roughness of the sample surface. The diffraction patterns are instantaneously displayed on the fluorescent screen located on the diametrically opposite side of the vacuum chamber from the electron gun. In this configuration, the growing surface can be continuously monitored during the sample growth.

the degree of inversion symmetry breaking (ISB) by designing new types of the superlattices. In this section, we first discuss the advantages of our MBE technology for the fabrication of Kondo superlattices. After that, we discuss the conditions for the realization of 2D Kondo lattice. We will also introduce three types of superconducting Kondo superlattices which we have fabricated so far: AB-, ABAB'-, and ABC-type superlattices, as shown in Fig. 3.

A. Molecular beam epitaxy (MBE) systems

MBE is a versatile technique for epitaxial growth by impinging molecular beams of atoms onto a heated substrate under ultra-high vacuum conditions ($\sim 10^{-7}$ Pa). The schematic of the basic evaporation process in the MBE chamber is shown in Fig. 2. In the following, we briefly introduce the main features of MBE method and our ultimate choice of MgF₂ substrate, which are key factors for the successful fabrication of multilayers of CeIn₃

and CeCoIn₅.

1. Features of MBE technology

The characteristic features of the MBE are described as follows. (1) The MBE is essentially a refined ultra-high vacuum evaporation method, which helps to prevent contaminations of the surface and oxidation of elements such as Ce; thus, high-quality thin films of Ce-based compounds can be grown using MBE. (2) MBE enables a slow growth rate of 0.01–0.02 nm/s that permits very precise control of layer thickness. Consequently, abrupt material interfaces can be achieved for fabrication of heterostructures such as superlattices. (3) The typical pressure in the MBE chamber is maintained at $\leq 10^{-7}$ Pa during the fabrication of thin films, which enables powerful diagnostic techniques, such as reflection high energy electron diffraction (RHEED), for *in situ* monitor of thin films growth without the complication of surface degradation. Thus, MBE technology is well-suited for achieving our goal of designing Kondo superlattices for dimensionality tuning of strongly correlated electron system.

2. MgF₂ substrate

There are several significant factors affecting the growth of thin films. Among them, lattice matching between the substrate and the thin film is considered to be one of the most crucial factors for epitaxial growth. Magnesium fluoride (MgF₂) has a rutile-type tetragonal structure with a lattice parameter $a = 0.462$ nm, which matches the lattice parameter $a = 0.468$ nm and $a = 0.461$ nm for CeIn₃ and CeCoIn₅, respectively. Furthermore, since MgF₂ does not contain oxygen, the oxidation of Ce-compounds during the growth can be avoided. Thus, single crystal MgF₂ is a suitable substrate material to support the epitaxial growth of CeIn₃ and CeCoIn₅ thin films.

The preparation of a clean MgF₂ substrate is another important factor in MBE deposition. First, atomically smooth MgF₂ surface is prepared by chemical mechanical polishing technologies. We purchased it in Crystal base Ltd. Next, the substrate is loaded into a high vacuum sample transfer area after cleaning by compressed air. Subsequently, the substrate is transferred to the MBE growth chamber, in which it is baked at 750°C for 2 hours to remove most contaminants from the substrate surface. Finally, the substrate temperature is reduced to about 550°C, which is the optimal growth temperature. After baking, a clear streak pattern of the MgF₂ substrate appears in the RHEED image, which indicates that the substrate has a very smooth and crystalline surface.

B. 2D Kondo lattice

To realize a 2D Kondo lattice, we fabricated the superlattices with alternating block layers (BLs) of n unit-cell-thick (UCT) Ce-compound and m -UCT non-magnetic compound, such as CeIn₃(n)/LaIn₃(m), CeCoIn₅(n)/YbCoIn₅(m), and CeRhIn₅(n)/YbRhIn₅(m) superlattices. In these superlattices, each Ce-BL can be treated as an isolated 2D Kondo lattice when the following two conditions are satisfied. (i) Ce-BLs are magnetically isolated from each other when non-magnetic-BLs with $m \gtrsim 2$ are inserted. This is achievable because the interlayer magnetic interaction mediated through the RKKY interaction between the Ce ions in different BLs reduces to less than $1/(m+1)^3$ of that between the neighboring Ce ions within the same layer.¹¹⁰ (ii) The dimensionality of each Ce-BL is reduced from three to two by forming the Ce-BL with a few unit-cell thickness ($n \lesssim 5$). Thus, 2D Kondo lattice can be achieved by using Kondo superlattice.

C. Superconducting Kondo superlattices

One of our primary interests is to develop a scheme to control the degree of ISB through an appropriate design of Kondo superlattices. We have succeeded in designing and fabricating several types of superconducting superlattices, namely AB-, ABAB'-, and ABC-type superlattices. These superlattices all contain heavy fermion superconductor CeCoIn₅ and conventional metals YbCoIn₅ and/or YbRhIn₅.

The AB-type superlattice is a conventional superlattice with alternating BLs of n -UCT CeCoIn₅ and m -UCT YbCoIn₅ or YbRhIn₅, forming an ($n:m$) heterostructure. Spatial inversion symmetry is locally broken at the top and the bottom “interface” CeCoIn₅ layers in the immediate proximity to the Yb-BLs, which induces an asymmetric potential gradient associated with the local ISB, $-\nabla V_{\text{local}}$,^{35,111} as indicated by the green (small) arrows in Fig. 3(a). In this case, the Fermi surface is split into two sheets with different spin structures: the spin direction is tilted into the plane, rotating clockwise on one sheet and anti-clockwise on the other. Since the fraction of noncentrosymmetric interface layers increases rapidly with the reduction of the thickness of Ce-BL, the effect of this “local ISB” is expected to be more pronounced with decreasing n .

The ABAB'-type superlattice is a modulated superlattice, which consists of n -UCT CeCoIn₅ sandwiched by m - and m' -UCT YbCoIn₅ or YbRhIn₅, denoted as an ($n:m:n:m'$) superlattice. In this superlattice, an inversion symmetry is broken in all of Ce-planes through the thickness modulation of Yb-BL,³⁶ in addition to the local ISB. The asymmetric potential gradient associated with the Yb-BL thickness modulation, $-\nabla V_{\text{block}}$, points to the opposite direction in the neighboring CeCoIn₅-BLs

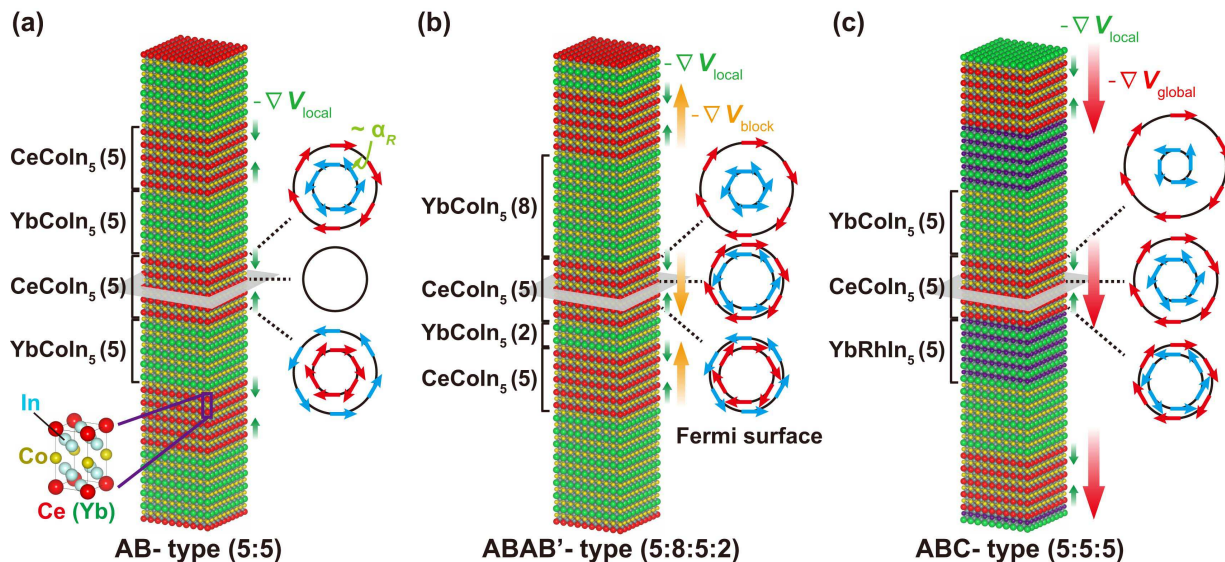


FIG. 3. Schematic representations of three types of superconducting Kondo superlattices. (a) AB-type: Superlattice with alternating layers of 5-UCT CeCoIn₅ and 5-UCT YbCoIn₅, $(n:m) = (5:5)$. The middle CeCoIn₅ layer in a given CeCoIn₅ block layer indicated by the gray plane is a mirror plane. The green small arrows represent the asymmetric potential gradient associated with the local ISB, $-\nabla V_{\text{local}}$. The Rashba splitting, α_R , occurs at the interface CeCoIn₅ layers neighboring the YbCoIn₅ layers due to the local ISB. The spin direction is rotated in the ab plane and is opposite between the top and bottom CeCoIn₅ layers. (b) ABAB'-type: 5-UCT CeCoIn₅ block layers are sandwiched by 8- and 2-UCT YbCoIn₅ layers, $(n:m:n') = (5:8:5:2)$. The middle CeCoIn₅ layer (gray plane) is not a mirror plane. The orange medium arrows represent the asymmetric potential gradient associated with the YbCoIn₅ layer thickness modulation $-\nabla V_{\text{block}}$, which points to the opposite direction in the neighboring CeCoIn₅-BLs. (c) ABC-type: Tricolor superlattice consisting of 5-UCT CeCoIn₅, 5-UCT YbCoIn₅, and 5-UCT YbRhIn₅, $(n:m:l) = (5:5:5)$. All layers including the middle CeCoIn₅ layer (gray plane) are not a mirror plane. The asymmetric potential gradient (red large arrows) associated with global ISB faces the same direction for all CeCoIn₅-BLs.

as shown by the orange (medium) arrows in Fig. 3(b). We note that mirror planes can be found in Yb-BL even in the ABAB'-type superlattice; however, here we focus mainly on ISB in the Ce-planes. We expect that the degree of this “*block layer ISB*” can be enhanced with increasing $|m - m'|$, which represents the degree of thickness modulation of Yb-BLs.

The ABC-type superlattice is a tricolor superlattice composed of n -UCT CeCoIn₅, m -UCT YbCoIn₅, and l -UCT YbRhIn₅, forming an $(n:m:l)$ c -axis oriented superlattice structure. In this case, we find immediately that an inversion symmetry is globally broken along the c axis, as well as the local ISB. The asymmetric potential gradient associated with global ISB, $-\nabla V_{\text{global}}$, faces the same direction for all CeCoIn₅-BLs as shown by the red (large) arrows in Fig. 3(c), which is in stark contrast to the case of block layer ISB. We anticipate that the degree of this “*global ISB*” can be tuned by changing the ratio of the thickness of YbCoIn₅ to that of YbRhIn₅, m/l .

Thus, through fabrication of superlattices with precise control of material composition and layer thicknesses, three types of ISB can be introduced: local-, block layer-, and global-ISBs. In this report, we discuss the effect of local and/or block layer ISBs on the superconductivity and magnetic properties.

IV. TUNING THE QUANTUM CRITICALITY IN CEIN₃/LAIN₃ SUPERLATTICES

We first examine how the dimensionality of the Kondo lattice affects the AFM state. In reduced spatial dimensions, magnetic order is often suppressed due to quantum fluctuations. Therefore, the dimensionality can be regarded as a tuning parameter for quantum criticality. Here, to adjust the dimensionality in a controllable manner, we used MBE technique to grow AB-type superlattices with alternating layers of n -UCT CeIn₃ and m -UCT LaIn₃, forming an $(n:m)$ heterostructure.³³

A. Characterization of CeIn₃/LaIn₃ superlattices

The cross-sectional transmission electron microscope (TEM) image for the $(n:m) = (1:3)$ superlattice (Fig. 4(a)), in which the bright spots correspond to Ce atoms, provides direct evidence for the formation of the desired superlattice structure shown on the left hand side of the TEM image. The diffraction pattern of the electron beam incident along the $[110]$ direction shows clear superspots (Fig. 4(b)), which reflects the long-period stacking structures based the superlattices. The X-ray diffraction patterns (Fig. 4(c)) provide close agreement with the step model simulations¹¹² (green lines), demonstrating the re-

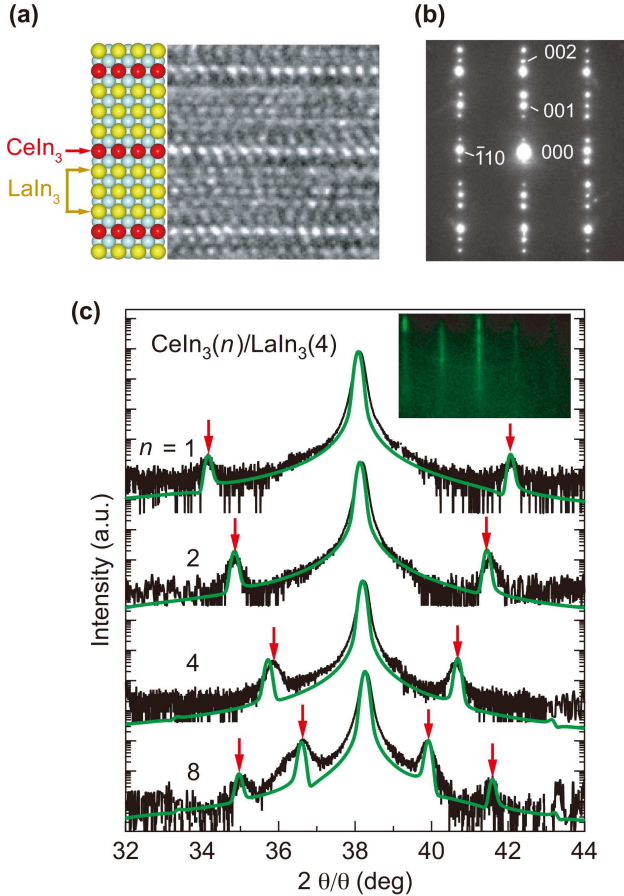


FIG. 4. Superlattice structure of CeIn_3 and LaIn_3 . (a) Cross-sectional TEM image of the $(n:m)=(1:3)$ superlattice. The Ce atoms can be identified as brighter spots than the La and In atoms. The left hand side image represents the designed $(1:3)$ superlattice structure. (b) The diffraction pattern of the electron beam incident along the $[110]$ direction. (c) X-ray diffraction patterns at around the (002) peak of the $(n:4)$ superlattices for $n = 1, 2, 4,$ and 8 . Green lines represent the step model simulations ignoring interface and layer-thickness fluctuations, which reproduces both the intensities and the positions of the satellite peaks (arrows). Inset: streak patterns of RHEED image of a typical $\text{CeIn}_3/\text{LaIn}_3$ superlattice.

alization of epitaxial superlattice structures, with no discernible inter-diffusion even for $n = 1$ cases. A clear streak pattern was also observed in the RHEED image (the inset of Fig. 4(c)), indicative of an epitaxial growth of each layer with atomic-scale flatness. Similar streak pattern is also observed in other superlattices, which confirms that epitaxial growth with smooth surfaces for all $(n:m)$ superlattices. These indicate the successful confinement of f -orbital electrons within the 2D space.

B. Suppression of Néel temperature with the dimensionality reduction

We investigate the transport properties of the $(n:m)$ superlattices as a function of CeIn_3 layer thickness n . As noted above, we set $m = 4$ to meet the requirement for realizing the 2D Kondo lattice, in which the interlayer magnetic interaction is substantially reduced. In fact, this 2D feature is manifested by the distinct anisotropy of the magnetoresistance for $(n:m)=(1:4)$, which is in sharp contrast to the magnetoresistance expected for both CeIn_3 and LaIn_3 , which possess a 3D isotropic structure.

Figures 5(a) and (b) show the temperature dependence of the in-plane resistivity normalized by its value at 10 K, $\rho(T)/\rho(10 \text{ K})$, and the Hall coefficient R_H for $\mathbf{H} \parallel c$, in each $(n:4)$ superlattice. For comparison, we also plot $\rho(T)$ of CeIn_3 thin film and $R_H(T)$ of bulk CeIn_3 , respectively. In CeIn_3 thin film, $\rho(T)$ reproduces well the result obtained in bulk single crystals; *i.e.*, $\rho(T)$ exhibits an increase owing to the Kondo scattering below $\sim 200 \text{ K}$, followed by a broad hump at $T_{\text{peak}} \sim 50 \text{ K}$, and a rapid decrease due to the suppression of the magnetic scattering after a distinct cusp at the Néel temperature $T_N = 10 \text{ K}$. In the superlattices, the hump structure becomes less pronounced with decreasing n , and $\rho(T)$ increases again below T_{peak} because of the interplay of the Kondo interaction with the crystal field effect,¹¹³ where energy scale is 123 K in CeIn_3 .¹¹⁴ At lower temperatures, $\rho(T)$ for $n \geq 3$ are essentially different from that for $n = 2$ and 1 . In the case of $n = 8, 6,$ and 3 , $\rho(T)$ shows a pronounced peak structure as indicated by arrows in Fig. 5(a). These peak temperatures coincide well with the temperatures at which $R_H(T)$ exhibit cusp-like minima (Fig. 5(b)) for $n = 8, 6,$ and 3 . Considering that both $\rho(T)$ and R_H have the cusp at T_N in CeIn_3 thin film, the observed transport anomalies for $n = 8, 6,$ and 3 appear as a result of AFM ordering. On the other hand, for $n = 2$ and 1 , $\rho(T)$ does not exhibit a clear peak, and $R_H(T)$ decreases monotonically with decreasing temperature without the upturn. These observations indicate that T_N is suppressed with decreasing CeIn_3 layer thickness, resulting in the disappearance of the AFM order near $n = 2$ (see Fig. 6(a)). It is thus natural to conclude that the enhanced AFM fluctuations associated with two-dimensionality are responsible for destroying this AFM order, as elaborated in the following section.

C. 2D antiferromagnetic QCP

The vanishing AFM order suggests the existence of a QCP close to $n = 2$, although the evidence from limited amount of data is not yet conclusive. In the vicinity of the QCP, quantum fluctuations cause the enhancement of the effective mass or the deviation from the Fermi liquid behavior.

First, we focus on the behavior of the effective mass.

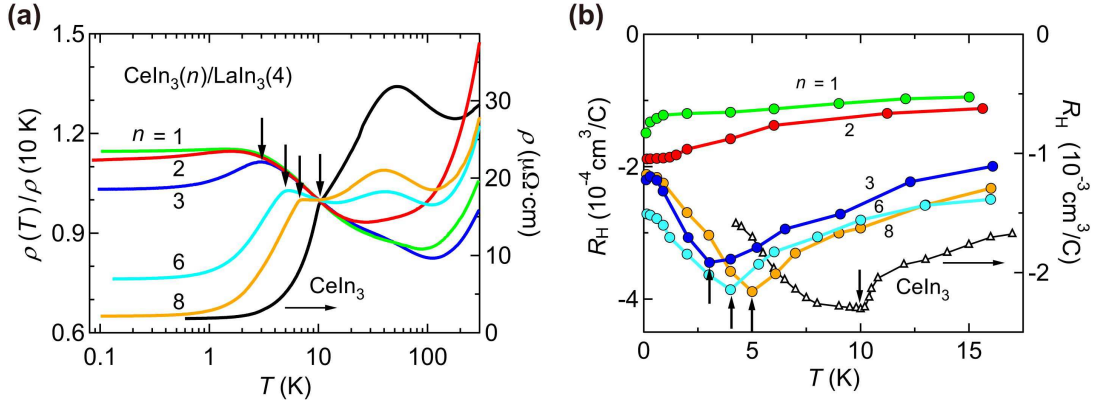


FIG. 5. Transport properties in the artificial superlattice $\text{CeIn}_3/\text{LaIn}_3$. (a) Temperature dependence of the resistivity normalized by its value at 10 K, $\rho(T)/\rho(10\text{ K})$, in the $(n:4)$ superlattices for $n = 1$ (green), 2 (red), 3 (dark blue), 6 (light blue), and 8 (yellow). The $\rho(T)$ of the CeIn_3 thin film (black line, right axis) coincides well with the bulk result. (b) Temperature dependence of the Hall coefficient R_H for the superlattices (left axis) and for bulk CeIn_3 (right axis). Both $\rho(T)$ and $R_H(T)$ show cusp-like behaviors (arrows) for $n = 8, 6$, and 3 as well as for CeIn_3 .

Away from the QCP, the resistivity follows the Fermi liquid behavior, $\rho(T) = \rho_0 + AT^\alpha$ with $\alpha = 2$, where ρ_0 is the residual resistivity and A is the Fermi liquid coefficient. Since the prefactor A is related to the Sommerfeld coefficient of specific heat γ by Kadowaki–Woods (KW) relation, $A = R_{\text{KY}}\gamma^2$ with $R_{\text{KY}} \sim 10^{-5} \mu\Omega\text{-cm (K}^2\text{-mol/mJ)}^2$,¹¹⁵ we can estimate the effective mass from the A value for $n \geq 3$, where T^2 -behavior is observed. As shown in Fig. 6(a), the prefactor A becomes larger with decreasing n , and consequently, the quasiparticle mass appears to be enhanced toward $n = 2$. Specifically, the γ value estimated from A is enhanced from the bulk CeIn_3 value of $\sim 120 \text{ mJ}/(\text{K}^2 \text{ mol})$ and reaches $\sim 350 \text{ mJ}/(\text{K}^2 \text{ mol})$ for $n = 3$, which corresponds to a quasiparticle mass at least several hundred times larger than the free electron mass. This mass enhancement indicates the existence of a QCP for $n < 3$.

An important question remains: what is the dimensionality and type of the QCP observed in $\text{CeIn}_3/\text{LaIn}_3$ superlattices? The temperature exponent α of the resistivity changes depending on the dimensionality and type of fluctuations in the vicinity of the QCP. Now, we examine α for $n = 2$, around which a QCP exists. As shown in Fig. 6(b), a T -linear dependence with $\alpha = 1.01 \pm 0.02$ is seen for $n = 2$, while the T^2 -dependence of ρ is observed at low temperatures for $n \geq 3$. The T -linear behavior is consistent with scattering by the fluctuations that are enhanced by the 2D-AFM QCP.⁴⁶ This is in contrast to the 3D case, where α is expected to be 1.5, and indeed $\alpha \sim 1.6$ is observed near the pressure-induced QCP in the bulk CeIn_3 .

For $n = 1$, the determination of α is challenging because of the weak temperature dependence of ρ . However, it has been reported that quantum criticality in strongly correlated electron systems can also be assessed by observing their properties under an external magnetic field.^{2,65,116} In fact, quantum criticality for $n = 2$ is removed by strong magnetic fields: the Fermi-liquid prop-

erties with $\alpha = 2$ are recovered, and simultaneously, the A value is quickly suppressed with an increasing magnetic field H (Fig. 6(a)). In the case of $n = 1$, the resistivity is also strongly modified by magnetic fields: a negative magnetoresistance is observed, which is consistent with the view that AFM fluctuations responsible for the scattering is suppressed by the magnetic field.

Thus, both the temperature and field dependencies of the transport properties in $\text{CeIn}_3/\text{LaIn}_3$ superlattices provide strong support for the presence of the quantum phase transition in the vicinity of $n = 2$, which is the outcome of dimensionality tuning. Furthermore, we conclude that the reduced dimensionality enhances the fluctuations associated with the 2D AFM QCP, and hence suppresses the magnetic order. The successful growth of epitaxial Ce-based superlattices promises to provide a setting for exploring the fundamental physics of strongly correlated electron systems such as the 2D Kondo lattice and, potentially, 2D superconductivity near a QCP.

V. 2D HEAVY FERMION SUPERCONDUCTOR OF $\text{CeCoIn}_5/\text{YbCoIn}_5$ SUPERLATTICES

We next investigate how the superconducting state evolves with the dimensionality reduction of the Kondo lattice. Although CeCoIn_5 is a candidate for 2D heavy fermion superconductor, all the electronic, magnetic, and superconducting properties measured in the bulk CeCoIn_5 are essentially 3D rather than 2D. Therefore, it is unclear whether superconductivity would persist upon the dimensionality reduction of the Kondo lattice from 3D to 2D. Here, we report on the observation of superconductivity in a strongly correlated system of heavy electrons confined within a 2D Kondo lattice,³⁴ which was realized by fabricating superconducting superlattices built of alternating layers of n -UCT CeCoIn_5 and m -UCT YbCoIn_5 , forming an $(n:m)$ heterostructure, *i.e.*,

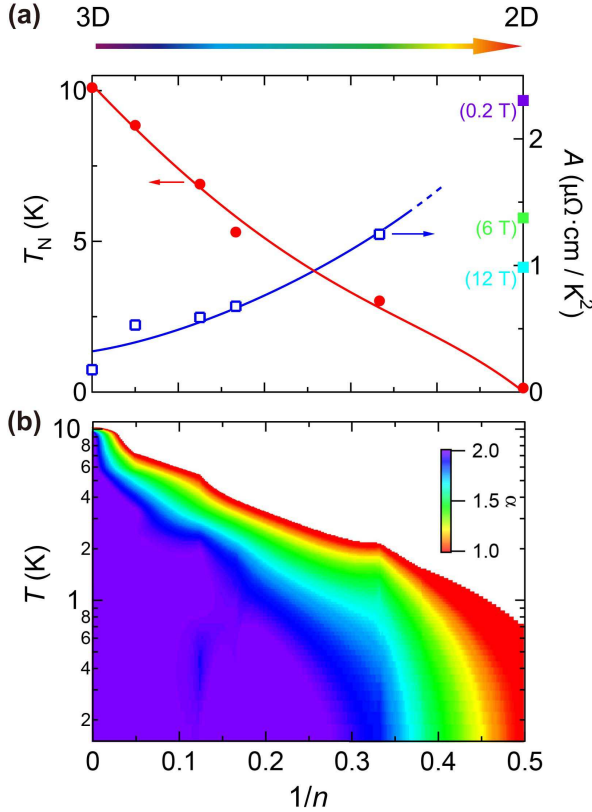


FIG. 6. Temperature versus dimensionality phase diagrams. (a) T_N (red circles) and the Fermi liquid coefficient A (open blue squares) as function of $1/n$. For $n = 2$, the A values are determined from $\rho(T)$ under magnetic fields (solid squares). The solid and dashed lines are guides for eyes. (b) Temperature and layer thickness evolution of the exponent α derived from the expression $\rho(T) = \rho_0 + AT^\alpha$.

AB-type superlattice. Here, we fix $m = 5$ to satisfy the condition for 2D Kondo lattice, in which the interlayer magnetic interaction is negligible small.

A. Characterization of CeCoIn₅/YbCoIn₅ superconducting superlattices

The high-resolution cross-sectional TEM result for the $(n:m)=(1:5)$ superlattice (Fig. 7(a)), in which the bright spots are identified as the Ce layers and the darker spots are Yb atoms, is consistent with the designed superlattice structure shown on the left hand side of the TEM image. The intensity integrated over the horizontal width of the TEM image indicates a clear difference between Ce and Yb layers, showing no discernible atomic interdiffusion between the neighboring Ce and Yb layers. The fast Fourier transform (FFT) of the TEM image (Figs. 7(b) and (c)) also shows clear superspots along the $[001]$ direction, which reflects the long-period stacking structure of the superlattices. Thus, the TEM results provide a clear evidence for the formation of $(n:m) = (1:5)$ superlattice. For all superlattices with different n val-

ues, the X-ray diffraction pattern (Fig. 7(d)) shows distinct lateral satellite peaks, demonstrating the continuous and evenly spaced CeCoIn₅ layers with no discernible inter-diffusion. The epitaxial growth of each layer with atomic flatness was confirmed by the streak pattern of the RHEED image (Fig. 7(e)). These results indicate the successful fabrication of epitaxial superlattices with sharp interfaces.

B. 2D heavy fermion superconductivity

We investigate the transport properties of the $(n:5)$ superlattices as a function of CeCoIn₅ layer thickness n . In a CeCoIn₅ thin film, the resistivity $\rho(T)$ (Fig. 8(a)) reproduces various features as observed in bulk single crystals well; *i.e.*, $\rho(T)$ shows an increase due to the Kondo scattering below ~ 100 K, followed by a maximum at the coherent temperature $T_{\text{coh}} \sim 40$ K, and a sharp drop at the superconducting transition. In the superlattices, the coherent peak is observed but it becomes less pronounced, particularly when n is reduced, as shown in Fig. 8(a). At lower temperatures, superconductivity with zero resistance is clearly observed in the superlattices for $n \geq 3$. On the other hand, for $n = 2$ and 1, $\rho(T)$ decreases below ~ 1 K but does not reach zero at the lowest temperature of our measurement. However, when the magnetic field is applied perpendicular to the layers for $n = 1$, $\rho(T)$ increases and recovers to the value extrapolated above 1 K at 5 T, whereas the reduction of $\rho(T)$ below 1 K remains in the parallel field of 6 T. Such large and anisotropic field response of $\rho(T)$ is typical for layered superconductors, demonstrating superconductivity even for $n = 1$.

Important questions are whether the superconducting electrons in the superlattices are heavy and if so what their dimensionality is. To answer these questions, we focus on the measurements of the upper critical field (H_{c2}) in CeCoIn₅/YbCoIn₅ superlattices. The orbital upper critical field at zero temperature for the field perpendicular to the layers, $H_{c2\perp}^{\text{orb}}(0)$, which reflects the effective electron mass in the plane, is estimated to be 6, 11, and 12 T for the $n = 3, 5,$ and 7 superlattices by the Werthamer–Helfand–Hohenberg (WHH) formula, $H_{c2\perp}^{\text{orb}}(0) = -0.69T_c(dH_{c2\perp}/dT)_{T_c}$.¹¹⁷ These magnitudes are comparable to or of the same order as $H_{c2\perp}^{\text{orb}}(0)$ ($= 14$ T) estimated in the bulk CeCoIn₅ single crystal, providing strong evidence that heavy f -electrons form Cooper pairs in the superlattices.

The superconducting order parameters of the CeCoIn₅-BLs are expected to be weakly coupled to each other by the proximity effect through the normal-metal YbCoIn₅-BLs. However, the proximity effect is negligible because the large Fermi velocity mismatch across the interface between CeCoIn₅ and YbCoIn₅ layers leads to a huge suppression of the transmission probability of electron currents.¹¹⁸ Therefore, when the thickness of the CeCoIn₅-BL is comparable to the perpendicular co-

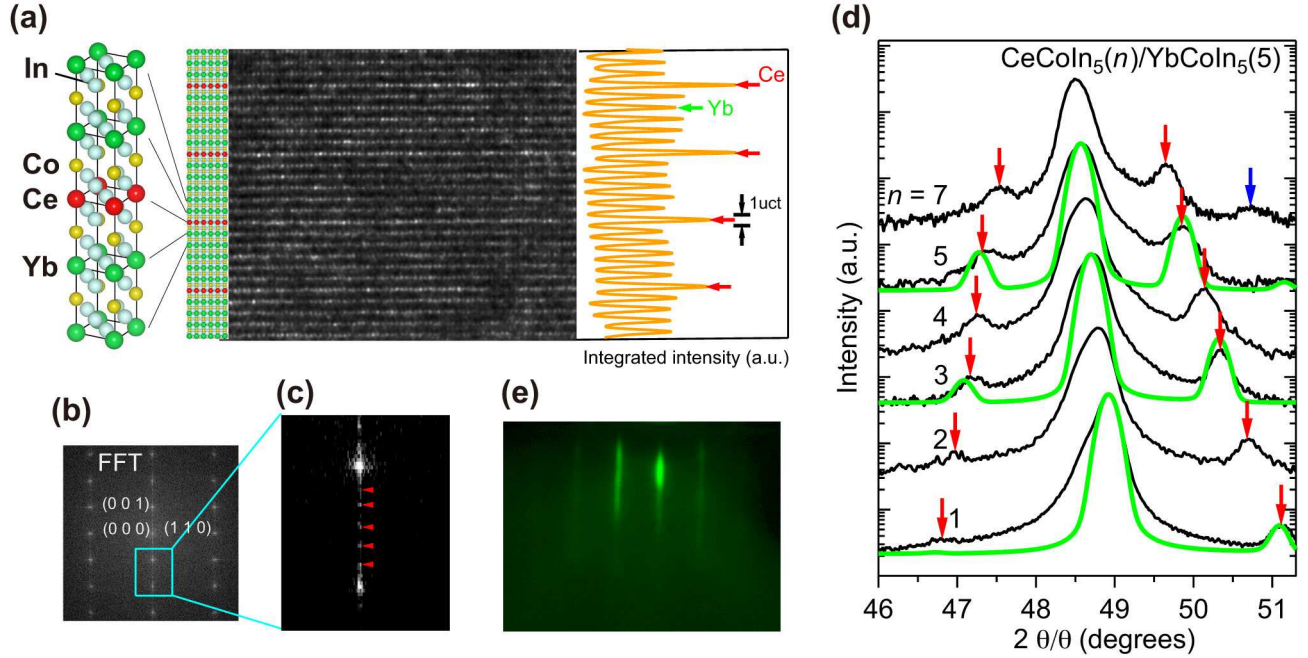


FIG. 7. Epitaxial superlattices ($n:5$) of $\text{CeCoIn}_5(n)/\text{YbCoIn}_5(5)$. (a) High-resolution cross-sectional TEM image of $n = 1$ superlattice. The bright dot arrays are identified as the Ce layers and the less bright dots are Yb atoms. The left panel of the TEM image represents the designed superlattice structure. The right panel represents the intensity integrated over the horizontal width of the TEM image plotted against vertical position. (b) The fast Fourier transform (FFT) of the TEM image. (c) Magnified view shows clear superspots along the $[001]$ direction. (d) $\text{Cu K}\alpha 1$ X-ray diffraction patterns of the ($n:5$) superlattices for $n = 1, 2, 3, 4, 5$ and 7 show first (red arrows) and second (blue arrow) satellite peaks. Both the positions and the asymmetric heights of the satellite peaks can be reproduced by the step-model simulations¹¹² (green lines), which neglect interface and layer-thickness fluctuations. (e) Streak patterns of the RHEED image during the growth.

herence length $\xi_{\perp} \sim 3\text{--}4$ nm for CeCoIn_5 (Ref. 74), each $\text{CeCoIn}_5\text{-BL}$ effectively acts as a 2D superconductor.¹¹⁹ Indeed, the 2D feature is revealed by the diverging $H_{c2\parallel}/H_{c2\perp}$ of the $n = 3, 5,$ and 7 superlattices on approaching T_c (Fig. 8(b)), in sharp contrast to the result observed in the bulk CeCoIn_5 (Ref. 48). Through these results, we can conclude that 2D heavy fermion superconductivity is realized in $\text{CeCoIn}_5(n)/\text{YbCoIn}_5(5)$ superlattices with $n = 3, 5,$ and 7 .

C. Enhancement of H_{c2}/T_c

We now discuss the 2D superconducting properties of $\text{CeCoIn}_5/\text{YbCoIn}_5$ superlattices. In the 2D limit, the angular dependence of the upper critical field, $H_{c2}(\theta)$, is generally described by the Tinkham model,¹²⁰ which follows a cusp-like dependence near the magnetic field parallel to the plane. However, at lower temperatures, $H_{c2}(\theta)$ of the $n = 3$ superlattice does not show the cusp structure and is qualitatively described by the anisotropic model¹²¹ (Fig. 8(c)). This fact implies that Pauli pair-breaking is dominant rather than orbital pair-breaking for the parallel magnetic field. Moreover, $H_{c2}(T)$ extrapolated to $T = 0$ K is significantly smaller than the estimated orbital-limited upper critical field $H_{c2\perp}^{\text{orb}}(0)$, indi-

cating a predominant Pauli paramagnetic pair-breaking effect even for the perpendicular field. Thus, 2D heavy fermion superconductivity of $\text{CeCoIn}_5/\text{YbCoIn}_5$ superlattices is also dominated by Pauli paramagnetism, similar to the case of the bulk CeCoIn_5 .

The most remarkable feature of this 2D heavy fermion superconductor is that T_c decreases rapidly from the bulk value with decreasing n , whereas H_{c2} values hardly change for both field directions at low temperatures. Indeed, H_{c2} of $n = 5$ and 7 is comparable to or larger than that of the bulk at low temperatures. This result immediately implies that the thickness reduction drastically enhances H_{c2}/T_c from the bulk value, as shown in Fig. 9. The pressure-dependence results,¹²² which is expected to make CeCoIn_5 more three-dimensional, also show a general trend of enhanced H_{c2}/T_c with reduced dimensionality although T_c has a dome shaped dependence. Until now, three hypotheses have been put forward to explain this trend: (a) extremely strong-coupling superconductivity, (b) Fulde-Ferrell-Larkin-Ovchinnikov (FFLO) state, and (c) locally non-centrosymmetric superconductivity. In the following, we briefly introduce the details of these scenarios.

(a) Extremely strong-coupling superconductivity

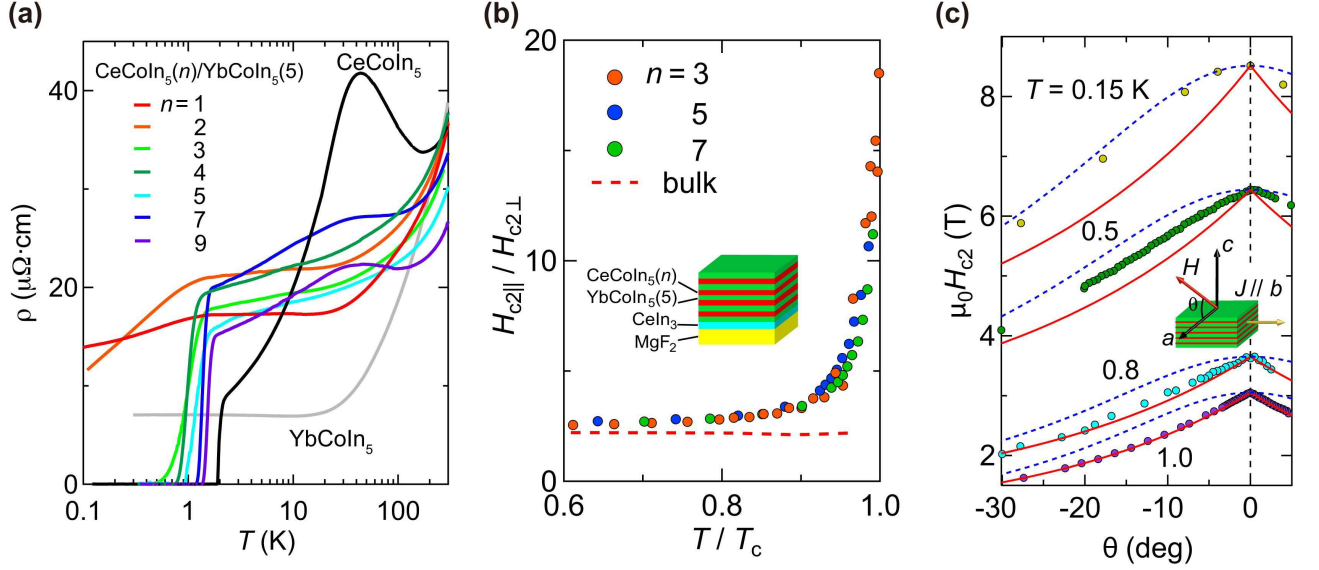


FIG. 8. Superconductivity in superlattices ($n:5$) of $\text{CeCoIn}_5(n)/\text{YbCoIn}_5(5)$. (a) Temperature dependence of the resistivity $\rho(T)$ for the $n = 1, 2, 3, 4, 5, 7, 9$ superlattices, along with those of CeCoIn_5 and YbCoIn_5 thin films with thickness of 300 nm. (b) Anisotropy of the upper critical field, $H_{c2\parallel}/H_{c2\perp}$, as a function of the reduced temperature, T/T_c , for the $n = 3, 5$, and 7 superlattices and for the bulk CeCoIn_5 . (c) Angular dependence of the upper critical field, $H_{c2}(\theta)$, at several temperatures. The dashed blue and solid red lines represent the fits to the data using the anisotropic model and the Tinkham model (see Eq. (2)), respectively.

In $\text{CeCoIn}_5/\text{YbCoIn}_5$ superlattices, H_{c2} is expected to be described by the Pauli-limited upper critical field H_{c2}^{P} , which is given by

$$H_{c2}^{\text{P}} = \sqrt{2}\Delta/g\mu_B, \quad (1)$$

where g is the gyromagnetic ratio determined by the Ce crystalline electric field levels. The g -value of the superlattices is assumed to deviate little from the bulk value because the anisotropy of H_{c2} at low temperatures does not depend on n , as shown in Fig. 8(b). In this case, via the relation given by Eq. (1), the striking enhancement of H_{c2}/T_c with decreasing n immediately implies a remarkable enhancement of Δ/T_c by two-dimensionalization. Using the reported value of $2\Delta/k_B T_c = 6$ in the bulk single crystal,⁸³ $2\Delta/k_B T_c$ for the $n = 5$ superlattice is estimated to exceed 10, which is significantly enhanced from the weak-coupling Bardeen–Cooper–Schrieffer value of $2\Delta/k_B T_c = 3.54$. This result is also supported by the theory that d -wave pairing mediated by antiferromagnetic fluctuations in 2D can be much stronger than that in 3D.^{125–127} Thus, extremely strong-coupling superconductivity may be realized in the 2D Kondo lattice.

(b) Fulde–Ferrell–Larkin–Ovchinnikov (FFLO) state

In the normal state, an external magnetic field splits the spin-up and spin-down states (Zeeman splitting); hence, the free energy of the system can be reduced by polarizing the spin of the electrons. On the other hand, spin-singlet Cooper pairs are not spin polarized by

the Zeeman effect because the pairs are formed between spin-up and spin-down electrons. Therefore, to polarize condensed electrons, Cooper pairs usually must be broken within the framework of the BCS theory, where the total momentum of the pairs is zero. However, if the formation of a new pairing state ($\mathbf{k} \uparrow, -\mathbf{k} + \mathbf{q} \downarrow$) with finite \mathbf{q} is realized, the system can lower its free energy even in the presence of a magnetic field. This state is called the FFLO state,^{94,95} which suppresses the Pauli pair-breaking effect.

The FFLO state is suggested to be more stable when a large area of the spin-up Fermi surface is connected to the spin-down surface by the \mathbf{q} -vector.¹²⁸ This bears a striking resemblance to the nesting effect of charge-density-wave (CDW) and spin-density-wave (SDW) transitions. For a 3D system with a spherical Fermi surface, the spin-down and spin-up Fermi surfaces touch only at a point by a shift of the \mathbf{q} -vector. For a 2D system with a cylindrical Fermi surface, the two Fermi surfaces touch on a line by a shift of the \mathbf{q} -vector. Therefore, two-dimensionality generally favors the FFLO state, leading to the suppression of Pauli paramagnetic pair-breaking.

(c) Locally non-centrosymmetric superconductivity

In the absence of space inversion symmetry, an asymmetric potential gradient ∇V yields a spin-orbit interaction.¹²⁹ For instance, asymmetry of the potential in the direction perpendicular to the 2D plane $\nabla V \parallel [001]$ induces Rashba spin-orbit interaction,¹³⁰ $\alpha_R \mathbf{g}(\mathbf{k}) \cdot \boldsymbol{\sigma} \propto$

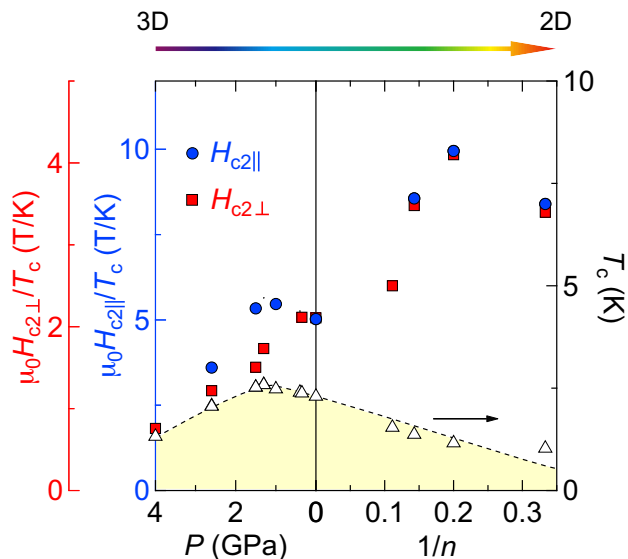


FIG. 9. Superconducting transition temperature, T_c (open triangles), and the upper critical fields divided by the transition temperature, H_{c2}/T_c , in parallel (filled blue circles) and perpendicular (filled red squares) fields as a function of dimensionality parameter $1/n$ (right panel). The pressure dependence of these quantities is also shown for comparison (left panel). The dimensionality is expected to increase with the pressure. Note the different scales for the parallel (blue) and the perpendicular (red) fields.

$(\mathbf{k} \times \nabla V) \cdot \boldsymbol{\sigma}$, where $\mathbf{g}(\mathbf{k}) = (-k_y, k_x, 0)/k_F$, k_F is the Fermi wave number, and $\boldsymbol{\sigma}$ is the Pauli matrix. The Rashba interaction splits the Fermi surface into two sheets with different spin structures: the spin direction is tilted into the plane, rotating clockwise on one sheet and anticlockwise on the other. In this case, the Zeeman interaction for magnetic field can be well approximated by $\pm \mathbf{g}(\mathbf{k}) \cdot \mu_0 \mathbf{H}$, leading to a strong suppression of the Pauli effect, in particular for $\mathbf{H} \parallel c$ where $\mathbf{g}(\mathbf{k})$ is always perpendicular to \mathbf{H} .^{131–133}

Recently, it has been proposed that local ISB at the interfaces of multilayer systems also suppresses Pauli pair-breaking effect when the interlayer hopping integral is comparable to or smaller than the Rashba splitting ($t_c \lesssim \alpha_R$).¹¹¹ The reason is that, since their coupling is expected to be weak due to the violation of spin and momentum conservation, noncentrosymmetric interface layers and centrosymmetric inner layers can be treated independently. In the CeCoIn₅/YbCoIn₅ superlattice, the inversion symmetry is *locally* broken at the top and the bottom “interface” CeCoIn₅ layers in the immediate proximity to the YbCoIn₅ BLs,³⁵ as illustrated in Fig. 3(a). Although the inner layers might also break the local inversion symmetry, the effect has been theoretically shown to be much weaker. Thus, with the reduction of n , the fraction of noncentrosymmetric interface layers increases rapidly. In the presence of the local ISB, coupled with the fact that Ce has a large atomic number, Rashba-

type spin-orbit coupling is expected to be strong, which appears to satisfy the condition $t_c \lesssim \alpha_R$. Therefore, the enhancement of spin susceptibility in the superconducting state have been predicted with decreasing n , leading to the suppression of the Pauli pair-breaking effect. At present, this scenario is the prevailing one for the enhancement of H_{c2}/T_c , as indicated in the next topic.

D. Local inversion symmetry breaking

Recently, the importance of the local inversion symmetry break (ISB) for the superconducting state has been emphasized experimentally through the anomalous temperature and angular dependencies of H_{c2} ,^{35,36} which can be interpreted as a strong suppression of the Pauli pair-breaking effect. Most recent site-selective NMR spectroscopy has also pointed out that the local ISB affects the magnetic properties, leading to the suppression of AFM fluctuations.³⁷ Thus, the interfacial effect becomes a key element for understanding the electronic state in the CeCoIn₅/YbCoIn₅ superlattices. The details of these experiments are given below.

1. Superconducting properties

Figure 10(a) shows the temperature dependence of the perpendicular upper critical field, $H_{c2\perp}$, normalized by $H_{c2\perp}^{\text{orb}}(0)$ for the superlattices CeCoIn₅(n)/YbCoIn₅(5) with $n = 3, 5$, and 7. We also include two extreme cases: $H_{c2\perp}/H_{c2\perp}^{\text{orb}}(0)$ for the bulk CeCoIn₅, in which superconductivity is dominated by Pauli paramagnetism,⁴⁸ and the WHH curve without the Pauli effect.¹¹⁷ A remarkable feature is that $H_{c2\perp}/H_{c2\perp}^{\text{orb}}(0)$ is enhanced with decreasing n in a wide temperature range. This is unlikely to be attributed to the impurity scattering because Yb substitution for Ce site in the bulk Ce_{1-x}Yb_xCoIn₅ system does not change the overall temperature dependence of $H_{c2\perp}/H_{c2\perp}^{\text{orb}}(0)$. We can also exclude the possibility that this enhancement is related to the dimensionality of the superconductivity, since $H_{c2\perp}/H_{c2\perp}^{\text{orb}}(0)$ varies with n even at $T \sim 0.8T_c$, where $\xi_{\perp}(T)$ is significantly longer than the Ce-BL thickness for all superlattices. The enhancement is rather associated with the reduction of the Maki parameter α_M , which represents the ratio of the orbital-limited upper critical field to that of the Pauli-limited case, although spin-orbit scattering may change a little with n . Thus, the enhanced $H_{c2\perp}/H_{c2\perp}^{\text{orb}}(0)$ with decreasing n indicates that the local ISB, whose degree is enhanced with decreasing n , modifies the superconducting properties, leading to the relative suppression of the Pauli effect with respect to the orbital effect.

The suppression of the Pauli pair-breaking effect can be identified clearly by the angular dependence of $H_{c2}(\theta)$ (Fig. 10(b)), where θ is the angle between \mathbf{H} and the a -axis. For $n = 3$, the distinct cusp behavior is observed at $\theta = 0$, whereas for $n = 4$ the cusp structure is not

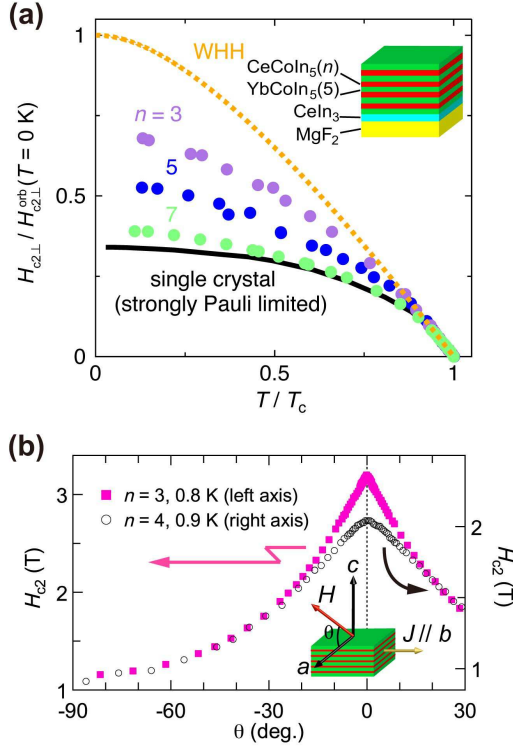


FIG. 10. Upper critical fields in the $\text{CeCoIn}_5(n)/\text{YbCoIn}_5(5)$ superlattices. (a) $H_{c2\perp}/H_{c2\perp}^{orb}(0)$ as a function of T/T_c for the $n = 3, 5$, and 7 superlattices. We also plot $H_{c2\perp}/H_{c2\perp}^{orb}(0)$ for CeCoIn_5 single crystal with strong Pauli effect and the WHH curve without the Pauli effect. (b) Comparison of $H_{c2}(\theta)$ for the $n = 3$ (pink filled squares, left axis) and $n = 4$ (black open circles, right axis) superlattices near T_c .

observed for all θ . This remarkable difference of $H_{c2}(\theta)$ between the $n = 3$ and $n = 4$ superlattices is highly unusual because the CeCoIn_5 BLs in each superlattice have the similar thickness, and, hence, similar angular variation of $H_{c2}(\theta)$ is expected, in particular near T_c where $\xi_{\perp}(T)$ well exceeds the CeCoIn_5 BL thickness. In order to describe the difference quantitatively, we analyze the data using the model below:³⁵

$$\left[\frac{H_{c2}(\theta) \cos \theta}{H_{c2}(0^\circ)} \right]^2 + \beta_T \left| \frac{H_{c2}(\theta) \sin \theta}{H_{c2}(90^\circ)} \right| + \beta_P \left[\frac{H_{c2}(\theta) \sin \theta}{H_{c2}(90^\circ)} \right]^2 = 1, \quad (2)$$

where β_T (≥ 0) and β_P (≥ 0) are fitting parameters with $\beta_T + \beta_P = 1$. $(\beta_T, \beta_P) = (1, 0)$ represents the so-called Tinkham model,¹²¹ which describes $H_{c2}(\theta)$ in a 2D thin film in the absence of the Pauli effect. In the Tinkham model, a cusp appears at $\theta = 0$ as a result of the vortex formation due to the orbital pair-breaking effect in a slightly tilted field, which strongly suppresses H_{c2} . On the other hand, $(\beta_T, \beta_P) = (0, 1)$ represents the anisotropic model, which describes $H_{c2}(\theta)$ of 2D superconductors with strong Pauli effect. In this case, a cusp does not appear because $H_{c2}(\theta)$ given by the relation of Eq. (1) is determined by the anisotropy of the g -factor,

which changes smoothly with θ . Therefore, β_T/β_P quantifies the relative contribution of orbital and Pauli paramagnetic effects. $H_{c2}(\theta)$ is well fitted with this model, and β_T/β_P is obtained. As depicted in Fig. 13(c), β_T/β_P is strongly enhanced with decreasing n , indicating the suppression of the Pauli effect. This result is consistent with the enhancement of $H_{c2\perp}/H_{c2\perp}^{orb}(0)$ with decreasing n shown in Fig. 10(a). Thus, both the enhancement of $H_{c2\perp}(T)/H_{c2\perp}^{orb}(T=0)$ in perpendicular field and the angular variation of $H_{c2}(\theta)$ around parallel field indicate that the local ISB has a strong impact on the superconductivity through the suppression of Pauli paramagnetism.

2. Magnetic properties

Figures 11(a) and 11(b) show the NMR spectra at 3.2 K near the In(1) central transition for the $n = 9$ and $n = 5$ superlattices. We can separate signals from three different layers by comparing the spectra with that of CeCoIn_5 and YbCoIn_5 thin films: the red, orange, and yellow shaded regions represent the spectra of CeCoIn_5 -BLs, the green regions the spectra of YbCoIn_5 -BLs, and the peak shown by an asterisk the spectra of CeIn_3 buffer layers. A notable feature is that, in the lower-field region, the spectrum of CeCoIn_5 -BLs for $n = 9$ has a much larger weight compared with that for $n = 5$. This naturally implies that the spectral regions shaded by yellow and red arise from the interface- and inner-layers of CeCoIn_5 -BLs, respectively, since the volume fraction of the interface layers increases rapidly with the reduction of n . Therefore, the field dependence of $(T_1T)^{-1}$ makes it possible to resolve the layer dependence of the AFM fluctuations even within the same CeCoIn_5 -BL because $(T_1T)^{-1}$ at the In(1) detects the magnitude of the fluctuations.

The field dependence of $(T_1T)^{-1}$ (Fig. 11(c)) indicates that AFM fluctuations near the interface are weaker than those at the inner layers of CeCoIn_5 -BLs. This strong spatial dependence implies that the interfacial effect plays a crucial role for determining the magnetic properties of the CeCoIn_5 -BLs. The proximity of f -electrons with magnetic moment to nonmagnetic YbCoIn_5 layers is unlikely to be the origin of the reduction of the fluctuations near interfaces, because magnetic fluctuations in the YbCoIn_5 -BLs are essentially the same as those in the YbCoIn_5 thin film. Therefore, the magnetic degrees of freedom of f -electrons are quenched inside the YbCoIn_5 -BLs. A possible explanation for the weakening of the AFM fluctuations is the effect of the local ISB at the interfaces between CeCoIn_5 - and YbCoIn_5 -BLs. In this case, the Fermi surface splitting due to the Rashba spin-orbit interaction should seriously change the nesting condition, and hence the commensurate AFM fluctuations with $\mathbf{Q} = (1/2, 1/2, 1/2)$, which is dominant in bulk CeCoIn_5 ,⁵² is expected to be suppressed. Moreover, it has been pointed out that the local ISB reduces

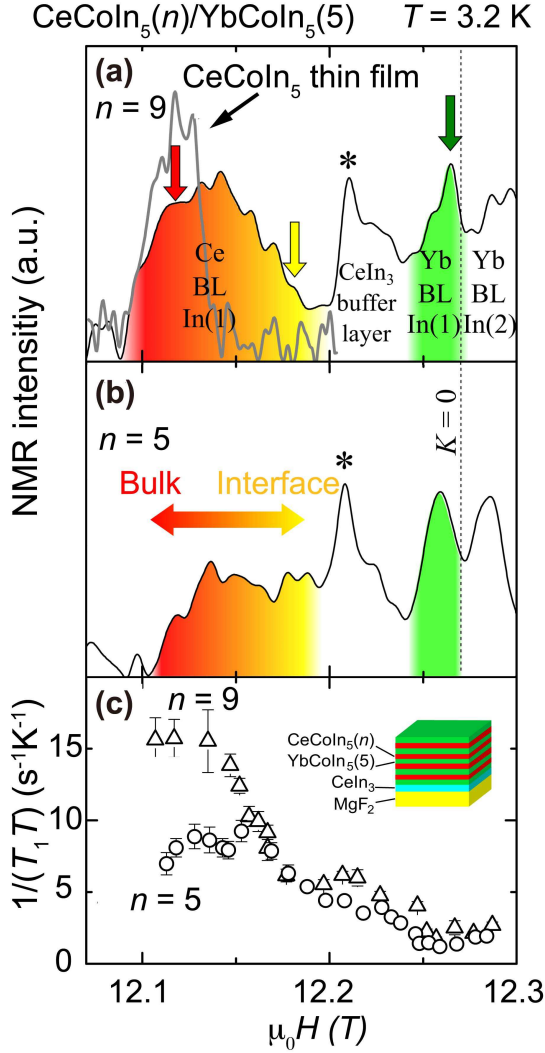


FIG. 11. Site-selective NMR measurements of the superlattices. (a), (b) $^{115}\text{In}(1)$ -NMR spectra of the $n = 9$ and 5 superlattices at $T = 3.2$ K and with fixed NMR frequency ($f = 114.5$ MHz). The red to yellow gradation represents the NMR signal from inner to interface layers in CeCoIn_5 -BLs. (c) Field dependence of $(T_1T)^{-1}$ in the $n = 9$ and 5 superlattices.

the AFM fluctuations by lifting the degeneracy of the fluctuation modes through the helical anisotropy of the spin configuration shown in Fig. 3(a).^{134,135} Therefore, the reduction of $(T_1T)^{-1}$ near interfaces implies the significance of the local ISB for the magnetic properties of $\text{CeCoIn}_5/\text{YbCoIn}_5$ superlattices.

To summarize this section, we have clarified that the $\text{CeCoIn}_5/\text{YbCoIn}_5$ superlattice shows the Pauli-limited superconductivity, in which heavy f -electrons confined within a 2D Kondo lattice form Cooper pairs. Moreover, from $H_{c2\perp}(T)$, $H_{c2}(\theta)$, and $(T_1T)^{-1}$ results, we have found that the local ISB at interfaces becomes a key factor for understanding both superconducting and mag-

netic properties in the $\text{CeCoIn}_5/\text{YbCoIn}_5$ superlattice, even though the global inversion symmetry is preserved in the whole crystals. This idea is also supported by very recent experiment of antiferromagnetic Kondo superlattices $\text{CeRhIn}_5/\text{YbRhIn}_5$,¹³⁶ in which the suppression of the Zeeman effect by local ISB helps to reduce the destruction of the AFM state under the magnetic field. Thus, the successful fabrication of $\text{CeCoIn}_5/\text{YbCoIn}_5$ superlattice pledges to be the first step toward understanding the combination of f -electron physics, superconductivity, and low dimensionality as well as interfacial effects. In fact, these complexities are expected to give rise to novel superconducting states in heavy fermion systems, such as the interplay of Kondo lattice physics and Berezinskii–Kosterlitz–Thouless (BKT) transition,¹¹⁸ dimensional-crossover in a heavy fermion superconductor,^{137,138} 2D FFLO phases,¹²⁸ and superconductivity accompanied by symmetry breaking not available in the bulk such as the local ISB.¹¹¹

VI. CONTROLLABLE RASHBA SPIN-ORBIT INTERACTION IN $\text{CECOIN}_5/\text{YBCOIN}_5$ SUPERLATTICES

To examine more widely how ISB affects the superconductivity of the 2D CeCoIn_5 BLs, we go a step further by fabricating *modulated* superlattices:³⁶ the thickness of CeCoIn_5 is now kept to $n = 5$ for the entire superlattice, while the thickness of YbCoIn_5 alternates between m and m' from one block layer to the next, forming an $(5:m:5:m')$ c -axis oriented superlattice structure. Here, we study superlattices both without and with thickness modulation of YbCoIn_5 layers, $m = m'$ (AB-type, Fig. 3(a)) and $m \neq m'$ (ABAB'-type, Fig. 3(b)), whose total number is fixed at $m + m' = 10$. In the former case, inversion symmetry is locally broken at the interfaces between CeCoIn_5 and YbCoIn_5 layers as described in the previous section, whereas in the latter case, an additional ISB, *i.e.*, “block layer” ISB, is introduced to the CeCoIn_5 BLs, in addition to the local ISB (see also the Sec. 3.C “Superconducting Kondo superlattices”).

A. Characterization of the modulated superlattices

Figure 12(a) shows the high-angle annular dark-field scanning transmission electron microscope (HAADF-STEM) results for the $(n:m:n:m') = (5:8:5:2)$ superlattice. The bright spots correspond to Yb atoms and the less bright spots are Ce atoms, which are consistent with the designed superlattice structure shown on the left hand side of the HAADF-STEM image. The intensity integrated over the horizontal width of the HAADF-STEM image shown on the right hand side of the HAADF-STEM image indicates a clear difference between Ce and Yb layers. Thus, the HAADF-STEM results demonstrate

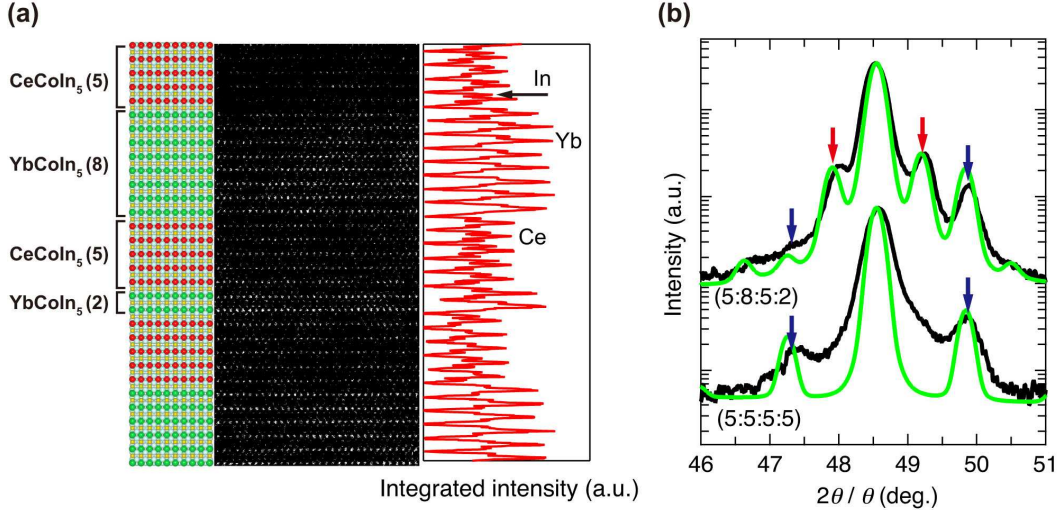


FIG. 12. Modulated superlattices ($5:m:5:m'$) of $\text{CeCoIn}_5(5)/\text{YbCoIn}_5(m)/\text{CeCoIn}_5(5)/\text{YbCoIn}_5(m')$. (a) HAADF-STEM image of the $(n:m:n:m') = (5:8:5:2)$ superlattice. The bright spots correspond to Yb atoms and the less bright spots are Ce atoms. The left hand side image represents the designed $(5:8:5:2)$ superlattice structure. Right panel represents the intensity integrated over the horizontal width of the HAADF-STEM image. (b) Cu $K\alpha 1$ X-ray diffraction patterns at around the (004) peak for $(n:m:n:m') = (5:5:5:5)$ and $(5:8:5:2)$ superlattices with a typical thickness of 300 nm. Two types of satellite peaks (marked by blue and red arrows) appear. Green lines represent the step model simulations ignoring interface and layer-thickness fluctuations.

the formation of a modulated superlattice, $(5:8:5:2)$ superlattice, with no discernible inter-diffusion.

The striking difference between the $(5:5:5:5)$ and $(5:8:5:2)$ superlattices is clearly observed in the X-ray diffraction pattern (Fig. 12(b)): the satellite peaks (marked by blue arrows) are observed in the $(5:5:5:5)$ superlattice, which reflects the long-period structures for AB-type superlattice, whereas extra satellite peaks (marked by red arrows) appear due to the thickness modulation of YbCoIn_5 in the $(5:8:5:2)$ superlattice. The position of the satellite peaks and their asymmetric heights can be reproduced by the step model simulation¹¹² (green lines) which does not include inter-diffusion, confirming the fabrication of both the $(5:5:5:5)$ and $(5:8:5:2)$ superlattices with sharp interfaces.

B. 2D superconducting state

We compare the transport properties of the ABAB'-type superlattices with $(n:m:n:m') = (5:7:5:3)$ and $(5:8:5:2)$ with those of the AB-type superlattice with $(n:m:n:m') = (5:5:5:5)$. The resistivity of the AB- and ABAB'-type superlattices exhibit a very similar temperature dependence. The residual resistivity $\rho_0 \simeq 16 \mu\Omega \text{ cm}$ is independent of the thickness modulation of YbCoIn_5 layers. These results imply that ISB does not affect the normal transport properties of the $\text{CeCoIn}_5/\text{YbCoIn}_5$ superlattices with a CeCoIn_5 thickness of 5 unit cell layers. At low temperatures, all superlattices show sharp resistive transitions to superconductivity, whose transition temperature T_c are almost similar to one another: 1.16,

1.18, and 1.13 K for $(n:m:n:m') = (5:5:5:5)$, $(5:7:5:3)$, and $(5:8:5:2)$, respectively. Moreover, the 2D superconducting feature is revealed by the diverging $H_{c2\parallel}/H_{c2\perp}$ of the superlattices on approaching T_c , in sharp contrast to the CeCoIn_5 thin film with a thickness of 120 nm.³⁶ Thus, these experimental evidences again suggest that 2D superconducting states are realized in $\text{CeCoIn}_5/\text{YbCoIn}_5$ superlattices, whether or not the inversion symmetry is present.

C. Block layer inversion symmetry breaking

We discuss the effect of Rashba splitting arising from block layer ISB on the 2D superconductivity. Figure 13(a) shows the temperature dependence of $H_{c2\perp}/H_{c2\perp}^{\text{orb}}(0)$ for $(n:m:n:m') = (5:5:5:5)$, $(5:7:5:3)$ and $(5:8:5:2)$, along with $H_{c2\perp}/H_{c2\perp}^{\text{orb}}(0)$ for the bulk CeCoIn_5 with strong Pauli effect⁴⁸ and the WHH curve without the Pauli effect.¹¹⁷ What is remarkable is that $H_{c2\perp}/H_{c2\perp}^{\text{orb}}(0)$ is enhanced with increasing $|m - m'|$ at low temperatures. This enhancement is not due to the difference in the electron scattering rate or impurity concentration because the resistivity of these superlattices shows a very similar temperature dependence with similar T_c . The enhancement is rather associated with the reduction in the ratio of the orbital- to Pauli-limited upper critical fields. Thus, the present results suggest that block layer ISB changes the superconducting properties, leading to the relative suppression of the Pauli effect with respect to the orbital effect.

To further investigate the role of the block layer ISB,

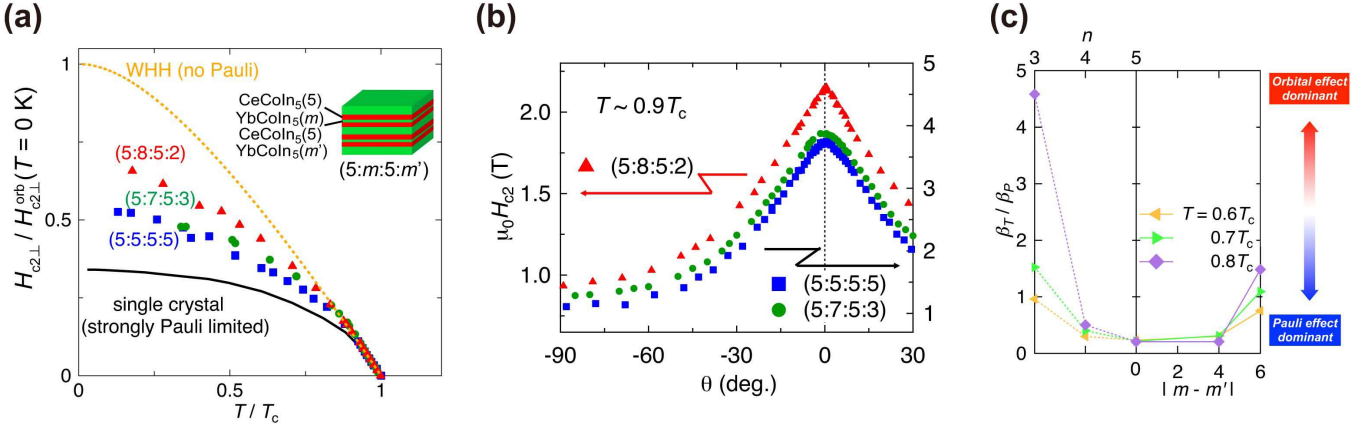


FIG. 13. Upper critical fields in the ABAB' superlattices. (a) $H_{c2\perp}/H_{c2\perp}^{orb}(0)$ versus T/T_c for $(n:m:n:m') = (5:5:5:5)$, $(5:7:5:3)$, and $(5:8:5:2)$ superlattices, along with that for CeCoIn_5 single crystal with strong Pauli effect and the WHH curve without the Pauli effect. (b) Comparison of $H_{c2}(\theta)$ in $(5:8:5:2)$ (red triangles, left axis), $(5:7:5:3)$ (green circles, right axis) and $(5:5:5:5)$ (blue squares, right axis) superlattices at around $T = 0.9T_c$. (c) β_T/β_P , which quantifies the relative importance of the orbital and Pauli-paramagnetic pair-breaking effects, is plotted as a function of the thickness modulation of YbCoIn_5 layers $|m - m'|$ (right panel). For comparison, β_T/β_P in the AB-type superlattice $\text{CeCoIn}_5(n)/\text{YbCoIn}_5(5)$ is plotted as a function of n (left panel).

we measured the angular dependence of the upper critical field, $H_{c2}(\theta)$, where θ is the angle between \mathbf{H} and the a -axis. The clear difference of $H_{c2}(\theta)$ between AB-type $(5:5:5:5)$ and ABAB'-type $(5:8:5:2)$ superlattices is observed, as shown in Fig. 13(b): for the $(5:8:5:2)$ superlattice, $H_{c2}(\theta)$ increases monotonically without saturation as $|\theta|$ decreases and the distinct cusp behavior is observed at $\theta = 0$, while for the $(5:7:5:3)$ and $(5:5:5:5)$ superlattices, the cusp structure is not observed and $H_{c2}(\theta)$ is smooth for all θ . In order to be more quantitative, we analyze the data using the model given by Eq. (2). Figure 13(c) summarizes the β_T/β_P obtained by this model for several superlattices at fixed reduced temperatures. For the ABAB'-type superlattices, when going from $(5:7:5:3)$ to $(5:8:5:2)$, β_T/β_P is strongly enhanced, indicating the suppression of the Pauli effect. This result is consistent with the low-temperature enhancement of $H_{c2\perp}/H_{c2\perp}^{orb}(0)$ with increasing $|m - m'|$ shown in Fig. 13(a). Thus, both the enhancement of $H_{c2\perp}(T)/H_{c2\perp}^{orb}(T=0)$ in the perpendicular magnetic field and the angular variation of $H_{c2}(\theta)$ around the parallel field indicate that ISB arising from the thickness modulation of YbCoIn_5 layers strongly affects the superconductivity through the suppression of Pauli paramagnetism, when $|m - m'|$ is increased from 4 to 6. This result can be understood if Rashba splitting begins to exceed the superconducting gap energy when $|m - m'|$ reaches a threshold value between 4 and 6.

Rashba splitting arising from the ISB has been suggested to affect the superconductivity, leading to several novel phenomena such as anomalous magneto-electric effects¹³⁹ and topological superconducting states.^{140–142} Such phenomena are expected to be more pronounced in heavy fermion systems due to the presence of strong

electron correlation effect.¹⁴³ Bulk CeCoIn_5 is one of the most attractive superconductors among these systems, because it exhibits many fascinating superconducting properties, as described in Sec. 2.B “Heavy fermion superconductor CeCoIn_5 ”. Therefore, our CeCoIn_5 -based superlattices, in which the degree of ISB and consequently the Rashba splitting are controllable, offer the prospect of achieving even more fascinating pairing states than the bulk CeCoIn_5 . In fact, it has been predicted theoretically that the availability of such superlattices provides an ideal playground for exploring exotic superconducting states, such as a helical vortex state,¹⁴⁴ pair-density-wave state,¹⁴⁵ complex-stripe phases,¹⁴⁶ parity-mixed superconductivity,¹⁴⁷ a topological crystalline superconducting state protected by mirror symmetry,^{148,149} and Majorana fermion excitations¹⁵⁰ in strongly correlated electron systems. Recently, the formation of Majorana flat band has also been proposed in the present ABAB'-type superlattice structure.¹⁵¹

VII. CONCLUSION

In this report, we have reviewed the development of the research in the 2D Kondo lattice systems, which can be realized by fabricating the Kondo superlattices. In the first Kondo superlattices $\text{CeIn}_3/\text{LaIn}_3$, the thickness reduction of the antiferromagnetic heavy fermion CeIn_3 layers leads to the suppression of the magnetic order and the enhancement of the effective mass, which both indicate the approaching to a QCP. In the vicinity of the QCP, the resistivity exhibits a non-Fermi liquid behavior with a linear temperature dependence, which is consistent with the scattering from quantum fluctuations

enhanced by the 2D-AFM QCP. Thus, we have found that the dimensionality reduction of the Kondo lattice suppresses 3D AFM state and surprisingly generates 2D AFM fluctuations rather than 3D ones.

In the superconducting Kondo superlattices CeCoIn₅/YbCoIn₅, heavy fermion superconductivity is realized even at single-unit-cell-thick layer of heavy fermion superconductor CeCoIn₅. The two-dimensionalization leads to the dramatic changes in the temperature and angular dependencies of the upper critical field. Moreover, by using the site-selective NMR measurements, we have found a significant reduction of the magnetic fluctuations at the interface CeCoIn₅ layers neighboring the YbCoIn₅ layers. These results can be well explained by the effect of the local ISB at the interfaces between CeCoIn₅ and YbCoIn₅ layers. Subsequent to this work, we have shown that the block layer ISB, which results from the thickness modulation of the YbCoIn₅ layers, also has an impact on the superconducting properties of the superlattices through the suppression of the Pauli effect. Thus, the entanglement of the local- and block layer-ISBs, and the two-dimensionalization in the CeCoIn₅/YbCoIn₅ superlattices offer the prospect of achieving even more fascinating superconducting states. Further studies would be required to clarify how exotic superconducting state is realized in this system by using various experimental techniques such as a combined STM-MBE system, site-selective NMR,³⁷ scanning SQUID microscopy, and terahertz spectroscopy.^{152,153}

Finally, we provide the most up-to-date status about

Kondo superlattices. Most recently, we have succeeded in fabricating two new superlattices: tricolor superlattice CeCoIn₅/YbCoIn₅/YbRhIn₅ which do not possess global inversion symmetry and a hybrid superlattice of heavy fermion superconductor CeCoIn₅ and antiferromagnetic heavy fermion CeRhIn₅. At the time of writing this report, we have found that the tricolor superlattices exhibit the $H_{c2\perp}(T)$ and $H_{c2}(\theta)$ behaviors similar to the case of local- and block layer ISBs, while the hybrid superlattice shows both T_N and T_c . These superlattices promise the possibility of further in-depth exploration of the role of ISB on superconductivity, and the interplay between AFM fluctuations and superconductivity.

ACKNOWLEDGMENTS

The authors acknowledge collaborations with H. Shishido, Y. Mizukami, T. Yamanaka, T. Watashige, K. Ishida, Y. Yanase, H. Kontani, T. Terashima, A. I. Buzdin, M. Yamashita, H. Ikeda, S. Yasumoto, D. Watanabe, K. Yasu, T. Kato, R. Endo, and R. Kobayashi. We also thank the following for helpful discussions: M. Izaki, N. Kawakami, H. Kurata, K. Miyake, A. Tanaka, R. Arita, A. V. Chubukov, M. J. Graf, P. A. Lee, N. P. Ong, S. A. Kivelson, T. Takimoto, I. Vekhter, V. Mineev, R. Ikeda, S. Fujimoto, A. Balatsky, M. Sigrist, R. Peters, and Y. Tada. This work was supported by Grant-in-Aids for Scientific Research (S), and on Innovative Areas “Topological Materials Science”.

-
- ¹ S. Sachdev, *Quantum Phase Transition* (Cambridge Univ. Press, Cambridge, 2000).
- ² P. Gegenwart, Q. Si, and F. Steglich, *Nature Phys.* **4**, 186 (2008).
- ³ T. Shibauchi, A. Carrington, and Y. Matsuda, *Annu. Rev. Condens. Matter Phys.* **5**, 113 (2014).
- ⁴ G. R. Stewart, *Rev. Mod. Phys.* **56**, 755 (1984).
- ⁵ D. Aoki, A. Huxley, E. Ressouche, D. Braithwaite, J. Flouquet, J.-P. Brison, E. Lhotel, and C. Paulsen, *Nature* **413**, 613 (2001).
- ⁶ N. T. Huy, A. Gasparini, D. E. de Nijs, Y. Huang, J. C. P. Klaasse, T. Gortenmulder, A. de Visser, A. Hamann, T. Görlach, and H. v. Löhneysen, *Phys. Rev. Lett.* **99**, 067006 (2007).
- ⁷ F. Joynt and L. Taillefer, *Rev. Mod. Phys.* **74**, 235 (2002).
- ⁸ F. Lévy, I. Sheikin, B. Grenier, and A. D. Huxley, *Nature* **309**, 1343 (2005).
- ⁹ K. Matsubayashi, T. Tanaka, A. Sakai, S. Nakatsuji, Y. Kubo, and Y. Uwatoko, *Phys. Rev. Lett.* **109**, 187004 (2012).
- ¹⁰ M. Tsujimoto, Y. Matsumoto, T. Tomita, A. Sakai, and S. Nakatsuji, *Phys. Rev. Lett.* **113**, 267001 (2014).
- ¹¹ H. Q. Yuan, F. M. Grosche, M. Deppe, C. Geibel, G. Sparn, and F. Steglich, *Science* **302**, 2104 (2003).
- ¹² J. G. Bednorz and K. A. Müller, *Z. Phys. B* **64**, 189 (1986).
- ¹³ A. Damascelli, Z. Hussain, and Z.-X. Shen, *Rev. Mod. Phys.* **75**, 473 (2003).
- ¹⁴ Y. Kamihara, H. Hiramatsu, M. Hirano, R. Kawamura, H. Yanagi, T. Kamiya, and H. Hosono, *J. Am. Chem. Soc.* **128**, 10012 (2006).
- ¹⁵ G. R. Stewart, *Rev. Mod. Phys.* **83**, 1589 (2011).
- ¹⁶ D. S. Hecht, L. Hu, and G. Irvin, *Adv. Mater.* **23**, 1482 (2011).
- ¹⁷ H. Ohta, S. Kim, M. Y. T. Mizoguchi, K. Nomura, S. Ohta, T. Nomura, Y. Nakanishi, Y. Ikuhara, M. Hirano, H. Hosono, and K. Koumoto, *Nature Mat.* **6**, 129 (2007).
- ¹⁸ Z. F. Ezawa, *Quantum Hall Effects: Recent Theoretical and Experimental Developments* (World Scientific Publishing Company; 3 edition, 2013).
- ¹⁹ H. Hegger, C. Petrovic, E. G. Moshopoulou, M. F. Hundley, J. L. Sarrao, Z. Fisk, and J. D. Thompson, *Phys. Rev. Lett.* **84**, 4986 (2000).
- ²⁰ C. Petrovic, P. G. Pagliuso, M. F. Hundley, R. Movshovich, J. L. Sarrao, J. D. Thompson, Z. Fisk, and P. Monthoux, *J. Phys.: Condens. Matter* **13**, L337 (2001).
- ²¹ C. Petrovic, R. Movshovich, M. Jaime, P. G. Pagliuso, M. F. Hundley, J. L. Sarrao, Z. Fisk, and J. D. Thompson, *Europhys. Lett.* **53**, 354 (2001).
- ²² Y. Haga, Y. Inada, H. Harima, K. Oikawa, M. Murakawa,

- H. Nakawaki, Y. Tokiwa, D. Aoki, H. Shishido, S. Ikeda, N. Watanabe, and Y. Ōnuki, *Phys. Rev. B* **63**, 060503 (2001).
- ²³ R. Settai, T. Takeuchi, and Y. Ōnuki, *J. Phys. Soc. Jpn.* **76**, 051003 (2007).
- ²⁴ G. q. Zheng, K. Tanabe, T. Mito, S. Kawasaki, Y. Kitaoka, D. Aoki, Y. Haga, and Y. Onuki, *Phys. Rev. Lett.* **86**, 4664 (2001).
- ²⁵ Y. Ida, R. Settai, Y. Ota, F. Honda, and Y. Ōnuki, *J. Phys. Soc. Jpn.* **77**, 084708 (2008).
- ²⁶ M. Neumann, J. Nyéki, B. Cowan, and J. Saunders, *Science* **317**, 1356 (2007).
- ²⁷ A. Ohtomo and H. Y. Hwang, *Nature* **427**, 423 (2004).
- ²⁸ A. Brinkman, M. Huijben, M. V. Zalk, J. Huijben, U. Zeitler, J. C. Maan, W. G. V. D. Wiel, G. Rijnders, D. H. A. Blank, and H. Hilgenkamp, *Nature Mat.* **6**, 493 (2007).
- ²⁹ N. Reyren, S. Thiel, A. D. Caviglia, L. F. Kourkoutis, G. Hammerl, C. Richter, C. W. Schneider, T. Kopp, A.-S. Rüetschi, D. Jaccard, M. Gabay, D. A. Muller, J.-M. Triscone, and J. Mannhart, *Science* **317**, 1196 (2007).
- ³⁰ W. C. Sheets, B. Mercey, and W. Prellier, *Appl. Phys. Lett.* **91**, 192102 (2007).
- ³¹ U. Lüders, W. C. Sheets, A. David, W. Prellier, and R. Frésard, *Phys. Rev. B* **80**, 241102(R) (2009).
- ³² A. David, R. Frésard, P. Boullay, W. Prellier, U. Lüders, and P.-E. Janolin, *Appl. Phys. Lett.* **98**, 212106 (2011).
- ³³ H. Shishido, T. Shibauchi, K. Yasu, T. Kato, H. Kontani, T. Terashima, and Y. Matsuda, *Science* **327**, 980 (2010).
- ³⁴ Y. Mizukami, H. Shishido, T. Shibauchi, M. Shimozawa, S. Yasumoto, D. Watanabe, M. Yamashita, H. Ikeda, T. Terashima, H. Kontani, and Y. Matsuda, *Nature Phys.* **7**, 849 (2011).
- ³⁵ S. K. Goh, Y. Mizukami, H. Shishido, D. Watanabe, S. Yasumoto, M. Shimozawa, M. Yamashita, T. Terashima, Y. Yanase, T. Shibauchi, A. I. Buzdin, and Y. Matsuda, *Phys. Rev. Lett.* **109**, 157006 (2012).
- ³⁶ M. Shimozawa, S. K. Goh, R. Endo, R. Kobayashi, T. Watashige, Y. Mizukami, H. Ikeda, H. Shishido, Y. Yanase, T. Terashima, T. Shibauchi, and Y. Matsuda, *Phys. Rev. Lett.* **112**, 156404 (2014).
- ³⁷ T. Yamanaka, M. Shimozawa, R. Endo, Y. Mizukami, H. Shishido, T. Terashima, T. Shibauchi, Y. Matsuda, and K. Ishida, *Phys. Rev. B* **92**, 241105(R) (2015).
- ³⁸ J. D. Thompson and Z. Fisk, *J. Phys. Soc. Jpn.* **81**, 011002 (2012).
- ³⁹ N. D. Mathur, F. M. Grosche, S. R. Julian, I. R. Walker, D. M. Freye, R. K. W. Haselwimmer, and G. G. Lonzarich, *Nature* **394**, 39 (1998).
- ⁴⁰ E. D. Bauer, H. O. Lee, V. A. Sidorov, N. Kurita, K. Gofryk, J.-X. Zhu, F. Ronning, R. Movshovich, and J. D. Thompson, *Phys. Rev. B* **81**, 180507 (2010).
- ⁴¹ D. Kaczorowski, A. P. Pikul, D. Gnida, and V. H. Tran, *Phys. Rev. Lett.* **103**, 027003 (2009).
- ⁴² J. M. Lawrence and S. M. Shapiro, *Phys. Rev. B* **22**, 4379 (1980).
- ⁴³ A. Benoit, J. Boucherle, P. Convert, J. Flouquet, J. Palteau, and J. Schweizer, *Solid State Commun.* **34**, 293 (1980).
- ⁴⁴ G. Knebel, D. Braithwaite, P. C. Canfield, G. Lapertot, and J. Flouquet, *Phys. Rev. B* **65**, 024425 (2001).
- ⁴⁵ S. Kawasaki, T. Mito, Y. Kawasaki, H. Kotegawa, G.-Q. Zheng, Y. Kitaoka, H. Shishido, S. Araki, R. Settai, and Y. Ōnuki, *J. Phys. Soc. Jpn.* **73**, 1647 (2004).
- ⁴⁶ T. Moriya and K. Ueda, *Adv. Phys.* **49**, 555 (2000).
- ⁴⁷ V. A. Sidorov, M. Nicklas, P. G. Paglione, J. L. Sarrao, Y. Bang, A. V. Balatsky, and J. D. Thompson, *Phys. Rev. Lett.* **89**, 157004 (2002).
- ⁴⁸ T. Tayama, A. Harita, T. Sakakibara, Y. Haga, H. Shishido, R. Settai, and Y. Onuki, *Phys. Rev. B* **65**, 180504(R) (2002).
- ⁴⁹ Y. Nakajima, K. Izawa, Y. Matsuda, S. Uji, T. Terashima, H. Shishido, R. Settai, Y. Ōnuki, and H. Kontani, *J. Phys. Soc. Jpn.* **73**, 5 (2004).
- ⁵⁰ Y. Kohori, Y. Yamato, Y. Iwamoto, T. Kohara, E. D. Bauer, M. B. Maple, and J. L. Sarrao, *Phys. Rev. B* **64**, 134526 (2001).
- ⁵¹ S. Zaum, K. Grube, R. Schäfer, E. D. Bauer, J. D. Thompson, and H. v. Löhneysen, *Phys. Rev. Lett.* **106**, 087003 (2011).
- ⁵² C. Stock, C. Broholm, J. Hudis, H. J. Kang, and C. Petrovic, *Phys. Rev. Lett.* **100**, 087001 (2008).
- ⁵³ Y. Kawasaki, S. Kawasaki, M. Yashima, T. Mito, G.-Q. Zheng, Y. Kitaoka, H. Shishido, R. Settai, Y. Haga, and Y. Ōnuki, *J. Phys. Soc. Jpn.* **72**, 2308 (2003).
- ⁵⁴ T. Park, M. J. Graf, L. Boulauvskii, J. L. Sarrao, and J. D. Thompson, *Proc. Natl. Acad. Sci. USA* **105**, 6825 (2008).
- ⁵⁵ H. Shishido, R. Settai, S. Araki, T. Ueda, Y. Inada, T. C. Kobayashi, T. Muramatsu, Y. Haga, and Y. Ōnuki, *Phys. Rev. B* **66**, 214510 (2002).
- ⁵⁶ L. D. Pham, T. Park, S. Maquilon, J. D. Thompson, and Z. Fisk, *Phys. Rev. Lett.* **97**, 056404 (2006).
- ⁵⁷ R. S. Kumar, A. L. Cornelius, and J. L. Sarrao, *Phys. Rev. B* **70**, 214526 (2004).
- ⁵⁸ J. D. Thompson, M. Nicklas, V. A. Sidorov, E. D. Bauer, R. Movshovich, N. Curro, and J. Sarrao, *J. Alloys Compounds* **408–412**, 16 (2006).
- ⁵⁹ G. Sparn, R. Borth, E. Lengyel, P. Pagliuso, J. Sarrao, F. Steglich, and J. Thompson, *Physica B* **319**, 262 (2002).
- ⁶⁰ H. Shishido, T. Ueda, S. Hashimoto, T. Kubo, R. Settai, H. Harima, and Y. Ōnuki, *J. Phys.: Condens. Matter* **15**, L499 (2003).
- ⁶¹ Y. Nakajima, H. Shishido, H. Nakai, T. Shibauchi, K. Behnia, K. Izawa, M. Hedo, Y. Uwatoko, T. Matsumoto, R. Settai, Y. Ōnuki, H. Kontani, and Y. Matsuda, *J. Phys. Soc. Jpn.* **76**, 024703 (2007).
- ⁶² M. Yashima, S. Kawasaki, Y. Kawasaki, G. q. Zheng, Y. Kitaoka, H. Shishido, R. Settai, Y. Haga, and Y. Ōnuki, *J. Phys. Soc. Jpn.* **73**, 2073 (2004).
- ⁶³ F. Ronning, C. Capan, A. Bianchi, R. Movshovich, A. Lacerda, M. F. Hundley, J. D. Thompson, P. G. Pagliuso, and J. L. Sarrao, *Phys. Rev. B* **71**, 104528 (2005).
- ⁶⁴ J. Paglione, M. A. Tanatar, D. G. Hawthorn, E. Boaknin, R. W. Hill, M. Sutherland, and L. Tallifer, *Phys. Rev. Lett.* **91**, 246405 (2003).
- ⁶⁵ A. Bianchi, R. Movshovich, C. Capan, and P. G. Pagliuso, *Phys. Rev. Lett.* **91**, 187004 (2003).
- ⁶⁶ A. Bianchi, R. Movshovich, I. Vekhter, P. G. Pagliuso, and J. L. Sarrao, *Phys. Rev. Lett.* **91**, 257001 (2003).
- ⁶⁷ J. Paglione, M. A. Tanatar, J.-P. Reid, H. Shakeripour, C. Petrovic, and L. Taillefer, arXiv:1406.0031.
- ⁶⁸ S. Singh, C. Capan, M. Nicklas, M. Rams, A. Gladun, H. Lee, J. F. DiTusa, Z. Fisk, F. Steglich, and S. Wirth, *Phys. Rev. Lett.* **98**, 057001 (2007).
- ⁶⁹ K. Izawa, K. Behnia, Y. Matsuda, H. Shishido, R. Settai, Y. Ōnuki, and J. Flouquet, *Phys. Rev. Lett.* **99**, 147005

- (2007).
- ⁷⁰ E. D. Bauer, C. Capan, F. Ronning, R. Movshovich, J. D. Thompson, and J. L. Sarrao, *Phys. Rev. Lett.* **94**, 047001 (2005).
- ⁷¹ F. Ronning, C. Capan, E. D. Bauer, J. D. Thompson, J. L. Sarrao, and R. Movshovich, *Phys. Rev. B* **73**, 064519 (2006).
- ⁷² G. Knebel, D. Aoki, and J. Flouquet, *C. R. Physique* **12**, 542 (2011).
- ⁷³ M. Kenzelmann, T. Strassle, C. Niedermayer, M. Sigrist, B. Padmanabhan, M. Zolliker, A. D. Bianchi, R. Movshovich, E. D. Bauer, J. L. Sarrao, and J. D. Thompson, *Science* **321**, 1652 (2008).
- ⁷⁴ S. Ikeda, H. Shishido, M. Nakashima, R. Settai, D. Aoki, Y. Haga, H. Harima, Y. Aoki, T. Namiki, H. Sato, and Y. Ōnuki, *J. Phys. Soc. Jpn.* **70**, 2248 (2001).
- ⁷⁵ R. Movshovich, M. Jaime, J. D. Thompson, C. Petrovic, Z. Fisk, P. G. Pagliuso, and J. L. Sarrao, *Phys. Rev. Lett.* **86**, 5152 (2001).
- ⁷⁶ R. J. Ormeno, A. Sibley, C. E. Gough, S. Sebastian, and I. R. Fisher, *Phys. Rev. Lett.* **88**, 047005 (2002).
- ⁷⁷ S. Özcan, D. M. Broun, B. Morgan, R. K. W. Haselwimmer, J. L. Sarrao, S. Kamal, C. P. Bidinosti, P. J. Turner, M. Raudsepp, and J. R. Waldram, *Europhys. Lett.* **62**, 412 (2003).
- ⁷⁸ K. Hashimoto, Y. Mizukami, R. Katsumata, H. Shishido, M. Yamashita, H. Ikeda, Y. Matsuda, J. A. Schlueter, J. D. Fletcher, A. Carrington, D. Gnida, D. Kaczorowski, and T. Shibauchi, *Proc. Natl. Acad. Sci. USA* **110**, 3293 (2013).
- ⁷⁹ N. J. Curro, B. Simovic, P. C. Hammel, P. G. Pagliuso, J. L. Sarrao, J. D. Thompson, and G. B. Martins, *Phys. Rev. B* **64**, 180514 (2001).
- ⁸⁰ H. Xiao, T. Hu, C. C. Almasan, T. A. Sayles, and M. B. Maple, *Phys. Rev. B* **76**, 224510 (2007).
- ⁸¹ K. Izawa, H. Yamaguchi, Y. Matsuda, H. Shishido, R. Settai, and Y. Onuki, *Phys. Rev. Lett.* **87**, 057002 (2001).
- ⁸² K. An, T. Sakakibara, R. Settai, Y. Onuki, M. Hiragi, M. Ichioka, and K. Machida, *Phys. Rev. Lett.* **104**, 037002 (2010).
- ⁸³ W. K. Park, J. L. Sarrao, J. D. Thompson, and L. H. Greene, *Phys. Rev. Lett.* **100**, 177001 (2008).
- ⁸⁴ A. D. Bianchi, M. Kenzelmann, L. DeBeer-Schmitt, J. S. White, E. M. Forgan, J. Mesot, M. Zolliker, J. Kohlbrecher, R. Movshovich, E. D. Bauer, J. L. Sarrao, Z. Fisk, C. Petrovic, and M. E. Eskildsen, *Science* **319**, 177 (2008).
- ⁸⁵ M. P. Allan, F. Massee, D. K. Morr, J. V. Dyke, A. W. Rost, A. P. Mackenzie, C. Petrovic, and J. Davis, *Nature Phys.* **9**, 468 (2013).
- ⁸⁶ B. B. Zhou, S. Misra, E. H. da Silva Neto, P. Aynajian, R. E. Baumbach, J. D. Thompson, E. D. Bauer, and A. Yazdani, *Nature Phys.* **9**, 474 (2013).
- ⁸⁷ G. Sarma, *J. Phys. Chem. Solids* **24**, 1029 (1963).
- ⁸⁸ K. Maki and T. Tsuneto, *Prog. Theo. Phys.* **31**, 945 (1964).
- ⁸⁹ H. A. Radovan, N. A. Fortune, T. P. Murphy, S. T. Hannahs, E. C. Palm, S. W. Tozer, and D. Hall, *Nature* **425**, 51 (2003).
- ⁹⁰ R. Okazaki, H. Shishido, T. Shibauchi, M. Konczykowski, A. Buzdin, and Y. Matsuda, *Phys. Rev. B* **76**, 224529 (2007).
- ⁹¹ Y. Tokiwa, E. D. Bauer, and P. Gegenwart, *Phys. Rev. Lett.* **109**, 116402 (2012).
- ⁹² T. Takeuchi, H. Shishido, S. Ikeda, R. Settai, Y. Haga, and Y. Ōnuki, *J. Phys.: Condens. Matter* **14**, L261 (2002).
- ⁹³ N. Oeschler, P. Gegenwart, M. Lang, R. Movshovich, J. L. Sarrao, J. D. Thompson, and F. Steglich, *Phys. Rev. Lett.* **91**, 076402 (2003).
- ⁹⁴ P. Fulde and R. A. Ferrell, *Phys. Rev.* **135**, A550 (1964).
- ⁹⁵ A. I. Larkin and Y. N. Ovchinnikov, *Sov. Phys. JETP* **20**, 762 (1965).
- ⁹⁶ D. Saint-James, G. Sarma, and E. J. Thomas, *Type II Superconductivity* (Pergamon, New York, 1969).
- ⁹⁷ Y. Kasahara, Y. Nakajima, K. Izawa, Y. Matsuda, K. Behnia, H. Shishido, R. Settai, and Y. Onuki, *Phys. Rev. B* **72**, 214515 (2005).
- ⁹⁸ T. Watanabe, Y. Kasahara, K. Izawa, T. Sakakibara, Y. Matsuda, C. J. van der Beek, T. Hanaguri, H. Shishido, R. Settai, and Y. Onuki, *Phys. Rev. B* **70**, 020506(R) (2004).
- ⁹⁹ C. Martin, C. C. Agosta, S. W. Tozer, H. A. Radovan, E. C. Palm, T. P. Murphy, and J. L. Sarrao, *Phys. Rev. B* **71**, 020503(R) (2005).
- ¹⁰⁰ C. Capan, A. Bianchi, R. Movshovich, A. D. Christianson, A. Malinowski, M. F. Hundley, A. Lacerda, and P. G. Pagliuso, *Phys. Rev. B* **70**, 134513 (2004).
- ¹⁰¹ K. Kakuyanagi, M. Saitoh, K. Kumagai, S. Takashima, M. Nohara, H. Takagi, and Y. Matsuda, *Phys. Rev. Lett.* **94**, 047602 (2005).
- ¹⁰² K. Kumagai, M. Saitoh, T. Oyaizu, Y. Furukawa, S. Takashima, M. Nohara, H. Takagi, and Y. Matsuda, *Phys. Rev. Lett.* **97**, 227002 (2006).
- ¹⁰³ B.-L. Young, R. R. Urbano, N. J. Curro, J. D. Thompson, J. L. Sarrao, A. B. Vorontsov, and M. J. Graf, *Phys. Rev. Lett.* **98**, 036402 (2007).
- ¹⁰⁴ G. Koutroulakis, J. M. D. Stewart, V. F. Mitrović, M. Horvatić, C. Berthier, G. Lapertot, and J. Flouquet, *Phys. Rev. Lett.* **104**, 087001 (2010).
- ¹⁰⁵ M. Kenzelmann, S. Gerber, N. Egetenmeyer, J. L. Gavilano, T. Strässle, A. D. Bianchi, E. Ressouche, R. Movshovich, E. D. Bauer, J. L. Sarrao, and J. D. Thompson, *Phys. Rev. Lett.* **104**, 127001 (2010).
- ¹⁰⁶ S. Gerber, M. Bartkowiak, J. L. Gavilano, E. Ressouche, N. Egetenmeyer, C. Niedermayer, A. D. Bianchi, R. Movshovich, E. D. Bauer, J. D. Thompson, and M. Kenzelmann, *Nature Phys.* **10**, 126 (2014).
- ¹⁰⁷ D. F. Agterberg, M. Sigrist, and H. Tsunetsugu, *Phys. Rev. Lett.* **102**, 207004 (2009).
- ¹⁰⁸ Y. Yanase and M. Sigrist, *J. Phys. Soc. Jpn.* **78**, 114715 (2009).
- ¹⁰⁹ K. Kumagai, H. Shishido, T. Shibauchi, and Y. Matsuda, *Phys. Rev. Lett.* **106**, 137004 (2011).
- ¹¹⁰ R. Peters, Y. Tada, and N. Kawakami, *Phys. Rev. B* **88**, 155134 (2013).
- ¹¹¹ D. Maruyama, M. Sigrist, and Y. Yanase, *J. Phys. Soc. Jpn.* **81**, 034702 (2012).
- ¹¹² E. E. Fullerton, I. K. Schuller, H. Vanderstraeten, and Y. Bruynseraede, *Phys. Rev. B* **45**, 9292 (1992).
- ¹¹³ S. Kashiba, S. Maekawa, S. Takahashi, and M. Tachiki, *J. Phys. Soc. Jpn.* **55**, 1341 (1986).
- ¹¹⁴ W. Knafo, S. Raymond, B. Fåk, G. Lapertot, P. C. Canfield, and J. Flouquet, *J. Phys.: Condens. Matter* **15**, 3741 (2003).
- ¹¹⁵ H. Kontani, *Rep. Prog. Phys.* **71**, 026501 (2008).
- ¹¹⁶ T. Shibauchi, L. Krusin-Elbaum, M. Hasegawa, Y. Kasahara, R. Okazaki, and Y. Matsuda, *Proc. Natl. Acad. Sci.*

- USA **105**, 7120 (2008).
- ¹¹⁷ N. R. Werthamer, E. Helfand, and P. C. Hohenberg, Phys. Rev. **147**, 295 (1966).
- ¹¹⁸ J.-H. She and A. V. Balatsky, Phys. Rev. Lett. **109**, 077002 (2012).
- ¹¹⁹ T. Schneider and A. Schmidt, Phys. Rev. B **47**, 5915 (1993).
- ¹²⁰ M. Tinkham, Phys. Rev. **129**, 2413 (1963).
- ¹²¹ M. Tinkham, *Introduction to Superconductivity* (McGraw-Hill, New York, 2nd ed, 1996).
- ¹²² G. Knebel, D. Aoki, J.-P. Brison, L. Howald, G. Lapertot, J. Panarin, S. Raymond, and J. Flouquet, Phys. Status Solidi B **247**, 557 (2010).
- ¹²³ B. S. Chandrasekhar, Appl. Phys. Lett. **1**, 7 (1962).
- ¹²⁴ A. M. Clogston, Phys. Rev. Lett. **9**, 266 (1962).
- ¹²⁵ T. Takimoto and T. Moriya, Phys. Rev. B **66**, 134516 (2002).
- ¹²⁶ R. Arita, K. Kuroki, and H. Aoki, Phys. Rev. B **60**, 14585 (1999).
- ¹²⁷ P. Monthoux and G. G. Lonzarich, Phys. Rev. B **63**, 054529 (2001).
- ¹²⁸ Y. Matsuda and H. Shimahara, J. Phys. Soc. Jpn. **76**, 051005 (2007).
- ¹²⁹ E. Bauer and M. Sigrist, *Non-Centrosymmetric Superconductors: Introduction and Overview* (Springer, Heidelberg, 2012).
- ¹³⁰ E. I. Rashba, Sov. Phys. Solid State **2**, 1109 (1960).
- ¹³¹ L. P. Gor'kov and E. Rashba, Phys. Rev. Lett. **87**, 037004 (2001).
- ¹³² P. A. Frigeri, D. F. Agterberg, A. Koga, and M. Sigrist, Phys. Rev. Lett. **92**, 097001 (2004).
- ¹³³ V. P. Mineev, Low Temp. Phys. **37**, 872 (2011).
- ¹³⁴ Y. Yanase and M. Sigrist, J. Phys. Soc. Jpn. **77**, 124711 (2008).
- ¹³⁵ T. Takimoto, J. Phys. Soc. Jpn. **77**, 113706 (2008).
- ¹³⁶ T. Ishii *et al.*, Preparation.
- ¹³⁷ Y. Tada, R. Peters, and M. Oshikawa, Phys. Rev. B **88**, 235121 (2013).
- ¹³⁸ Y. Tada and R. Peters, Phys. Rev. B **92**, 035129 (2015).
- ¹³⁹ C. K. Lu and S. Yip, Phys. Rev. B **78**, 132502 (2008).
- ¹⁴⁰ Y. Tanaka, T. Yokoyama, A. V. Balatsky, and N. Nagaosa, Phys. Rev. B **79**, 060505(R) (2009).
- ¹⁴¹ M. Sato and S. Fujimoto, Phys. Rev. B **79**, 094504 (2009).
- ¹⁴² X. L. Qi and S. C. Zhang, Rev. Mod. Phys. **83**, 1057 (2011).
- ¹⁴³ S. Fujimoto, J. Phys. Soc. Jpn. **76**, 051008 (2007).
- ¹⁴⁴ R. P. Kaur, D. E. Agterberg, and M. Sigrist, Phys. Rev. Lett. **94**, 137002 (2005).
- ¹⁴⁵ T. Yoshida, M. Sigrist, and Y. Yanase, Phys. Rev. B **86**, 134514 (2012).
- ¹⁴⁶ T. Yoshida, M. Sigrist, and Y. Yanase, J. Phys. Soc. Jpn. **82**, 074714 (2013).
- ¹⁴⁷ T. Yoshida, M. Sigrist, and Y. Yanase, J. Phys. Soc. Jpn. **83**, 013703 (2014).
- ¹⁴⁸ T. Yoshida, M. Sigrist, and Y. Yanase, Phys. Rev. Lett. **115**, 027001 (2015).
- ¹⁴⁹ T. Watanabe, T. Yoshida, and Y. Yanase, Phys. Rev. B **92**, 174502 (2015).
- ¹⁵⁰ M. Sato and S. Fujimoto, Phys. Rev. Lett. **105**, 217001 (2010).
- ¹⁵¹ N. F. Q. Yuan, C. L. M. Wong, and K. T. Law, Physica E **55**, 30 (2014).
- ¹⁵² M. Scheffler, T. Weig, M. Dressel, H. Shishido, Y. Mizukami, T. Terashima, T. Shibauchi, and Y. Matsuda, J. Phys. Soc. Jpn. **82**, 043712 (2013).
- ¹⁵³ U. S. Pracht, J. Simmendinger, M. Dressel, R. Endo, T. Watashige, Y. Hanaoka, M. Shimozawa, T. Terashima, T. Shibauchi, Y. Matsuda, and M. Scheffler, J. Mag. Mater. **400**, 31 (2016).